Termination of a continent-margin upwelling system at the Permian-Triassic boundary (Opal Creek, Alberta, Canada)

Shane D. Schoepfer[1]*
Charles M. Henderson[2]
Geoffrey H. Garrison[1]
Julien Foriel[3]
Peter D. Ward[1]
David Selby[4]
James C. Hower[5]
Thomas J. Algeo[6]
Yanan Shen[7]

[1] Department of Earth and Space Sciences, University of Washington, Seattle, WA 98195, U.S.A.
[2] Department of Geoscience, University of Calgary, Calgary, AB, Canada
[3] Department of Earth and Planetary Science, Washington University, St. Louis, MO 63130, U.S.A.
[4] Department of Earth Sciences, Durham University, Durham, DH1 3LE, U.K.
[5] Center for Applied Energy Research and Department of Earth & Environmental Sciences, University of Kentucky, Lexington, KY 40506, U.S.A.
[6] Department of Geology, University of Cincinnati, Cincinnati, OH 45221 U.S.A.
[7]Chinese Academy of Sciences Key Laboratory of Crust-Mantle Materials and Environments, School of Earth and Space Sciences, University of Science and Technology of China, Hefei 230026, China

ABSTRACT

Models of mass extinctions caused by greenhouse warming depend on the ability of warming to affect the oxygenation of the ocean, either through slowing circulation or changes in biological productivity and the organic carbon budget. Opal Creek, Alberta, Canada is a biostratigraphically continuous Permian-Triassic Boundary (PTB) section deposited in deep water on an outer shelf setting in the vast and understudied Panthalassic Ocean, along the western margin of Pangaea. The end-Permian extinction is here represented as the disappearance of the previously dominant benthic fauna (siliceous sponges). On the basis of nitrogen and reduced sulfur isotopes as well as productivity-sensitive trace elements, the Middle Permian at Opal Creek is interpreted as a highly productive coastal upwelling zone where vigorous denitrification and sulfate reduction occurred in a mid-water oxygen minimum. Similar conditions appear to have continued into the latest Permian until the onset of a euxinic episode represented by a discrete pyrite bed and several trace element indicators of high productivity. This euxinic pulse is followed by the extinction of benthic fauna and a shift in nitrogen and sulfur isotopes to more normal marine values, suggesting the cessation of coastal upwelling and the consequent weakening of the mid-water oxygen minimum. The Lower Triassic appears to be a dysoxic, relatively unproductive environment with a bottom water oxygen minimum. Rhenium-Osmium isotope systematics show a minimum of radiogenic Os near the main extinction event, which may be due to volcanic input, and increasingly radiogenic values approaching the PTB, possibly due to increased continental erosion. The Opal Creek system demonstrates

that, while the biogeochemical crisis in the latest Permian was capable of impacting the coastal upwelling modality of ocean circulation, a transient increase in productivity likely drove the system toward euxinia and, ultimately, extinction.

Key words: Permian; extinction; Panthalassic; marine productivity; upwelling; anoxia

1. Introduction

The latest Permian mass extinction (LPME), at ~252 Ma, was the greatest biodiversity crisis of the Phanerozoic (Erwin et al., 2002), fundamentally and permanently altering terrestrial and marine ecosystems (Benton et al., 2004; Bottjer et al., 2008). The trigger for this crisis is thought to have been eruption of the Siberian Traps flood basalts (Wignall, 2007; Reichow et al., 2009), which led to strong global warming as a consequence of emissions of CO_2 and possibly methane (Payne and Kump, 2007; Retallack and Jahren, 2008). Climatic warming or related effects led to perturbations of terrestrial environments, including changes in weathering patterns, aridification, vegetation loss, and fluvial drainage alteration (Retallack, 1999; Looy et al., 1999, 2001; Ward et al., 2000). In the marine realm, warming is thought to have been an important factor in reduced deepwater ventilation, a buildup of hydrogen sulfide, hypercapnia, seawater acidification, and depletion of certain nutrients such as nitrate (Knoll et al., 1996; Kump et al., 2005; Fraiser and Bottjer, 2007; Luo et al., 2011). The development of global greenhouse conditions at this time is paleontologically evident in the appearance of warm-climate floras at polar latitudes (Taylor et al., 2000), the demise of high-latitude, cool-water siliceous sponge communities (Henderson, 1997; Beauchamp and Baud, 2002), and a breakdown of temperature-based conodont provincialism (Mei and Henderson, 2001).

Direct evaluation of changes in Permian-Triassic ocean circulation patterns has proven difficult, owing to the relative paucity of preserved PTB sections from the Panthalassic Ocean, which covered some 70% of the globe at the time of the extinction (Fig. 1) and hence is central to investigations of global change related to the LPME. . Extant Panthalassic sections are limited to a few areas and depositional facies, including deep-sea cherts (Isozaki, 1994, 1997; Algeo et al., 2010, 2011b; Sano et al., 2010) and shallow atoll carbonates from Japan (Musashi et al., 2001), volcanic-arc slope sediments in New Zealand (Krull et al., 2000), and a series of deep-shelf or upper slope siliciclastic successions in western North America (Beauchamp and Baud, 2002; Wignall and Newton, 2003; Hays et al., 2007). Anoxic facies have been documented at widespread Permian-Triassic boundary (PTB) sections, leading some workers to infer that such redox changes were global in extent, and due to strongly reduced overturning circulation ("ocean stagnation") (Isozaki, 1994, 1997; Wignall and Twitchett, 1996, 2002). Paleoceanographic modeling studies have demonstrated that, while strong climatic warming could slow the meridional overturning circulation significantly, it would generally not be sufficient to generate the persistent, highly reducing conditions necessary to drive surface euxinia without a substantial increase in nutrient availability (Hotinski et al., 2001; Meyer et al. 2008). Modeling of paleoceanographic conditions at the PTB generally supports the hypothesis that overturning circulation persists despite extreme greenhouse conditions (Kiehl and Shields, 2005; Winguth and Maier-Reimer, 2005).

Recently, attention has focused on the role of increased nutrient inventories in ocean-surface waters, and consequent increases in marine primary productivity, in driving PTB oceans toward anoxia (Algeo et al., 2011a). This hypothesis has received support from studies demonstrating a substantial expansion of the mid-ocean oxygen-minimum zone in

100 periequatorial regions (Algeo et al., 2010, 2011b) as well as a steepening of shallow-to-deep
101 carbon isotopic gradients in epicratonic seas (Meyer et al., 2011; Song et al., in review).

102 [Insert Figure 1]

103 In this study, we examine changes along the eastern margin of the subtropical
104 Panthalassic Ocean between the Early Permian and Early Triassic. Our primary goal is to
105 test models of anoxia-development in the Panthalassic ocean by collecting field geochemical
106 evidence for changes in circulation and organic productivity rates during the PTB transition
107 interval. The site for this study is the Opal Creek section in southwestern Alberta, which
108 represents an outer-shelf or upper slope setting on the western margin of the North
109 American plate at a paleolatitude of ~30°N (Henderson, 1989, Richards, 1989). As shown
110 by both field data and paleoceanographic modelling, this region was characterized by
111 strong upwelling during much of the Permian (Ziegler et al., 1998, Beauchamp and Baud,
112 2002, Winguth and Maier-Reimer, 2005), a mode of circulation potentially sensitive to
113 global climate changes. A shift in ocean circulation patterns is suggested by major changes
114 in boreal marine biotas during the Late Permian (Henderson and Baud, 1997; Beauchamp
115 and Baud, 2002; Gates et al., 2004; Beauchamp et al., 2009), culminating in a regional
116 extinction of sponges in the late Changhsingian (Algeo et al., 2012), as well as a shift from
117 the enriched nitrogen isotope values characteristic of coastal upwelling zones to values
118 characteristic of more nitrogen-limited environments (Schoepfer et al. 2012). Here, we
119 present sulfur isotope and trace-element concentration data in order to (1) document
120 changes in redox conditions, productivity, and euxinia within the upwelling system of the
121 eastern subtropical Panthalassic Ocean during Early Permian to Early Triassic, and (2)
122 evaluate the relationship of changes in this region during the PTB transition to broader
123 changes in the global environment based on detailed biostratigraphic correlations
124 (Henderson et al., 1994; Henderson, 1997).

2. Geologic setting and biostratigraphy

The Opal Creek section is located in the Kananaskis Valley, in the foothills of the Canadian Rockies west of Calgary (Fig. 1). It comprises ~25 meters of Lower Permian through Lower Triassic strata assigned to the Johnston Canyon, Ranger Canyon, and Sulphur Mountain formations. Beds dip nearly vertically, with cherts and silicified siltstones forming prominent cliffs while more fissile siltstones are exposed in hill slopes (Fig. 2). The thermal maturity of the section is moderate, as shown by a conodont color alteration index (CAI) of ~2.5 (Schoepfer et al., 2012), equivalent to a maximum burial temperature of ~150°C (Tissot and Welte, 1984; Hunt, 1996). Similar maturity levels have been inferred for other PTB sections in the Canadian Western Sedimentary Basin on the basis of vitrinite reflectance (Radke et al., 1982), CAI (Utting et al., 2005), and biomarker studies (Hays et al., 2007).

[Insert Figure 2]

The Early Permian is represented by the Johnson Canyon Formation (Fig. 3), which is composed of silty dolostone containing abundant nodular phosphate layers. This unit exhibits lithologic cyclicity, likely as a consequence of glacio-eustatic fluctuations during the Early Permian, when ice is believed to have existed at the poles (Haq and Schutter, 2008).

The Middle Permian is represented by the Ranger Canyon Formation (RCF, Figs. 3-4), which (together with its stratigraphic equivalent, the Fantasque Formation) extends from southeastern British Columbia northward to the southern Mackenzie Fold Belt in the Yukon (Henderson, 1989). The Ranger Canyon, which is just 2.35 m thick at Opal Creek, consists of completely bioturbated, recrystallized spiculitic chert to cherty immature siltstone containing microcrystalline carbonate cements and some reworked chert and carbonate grains. The predominance of sponge spicules, abundance of phosphatic material

149 including abundant conodonts, and the absence of shallow-water sedimentary structures
150 (Henderson, 1997) suggest an outer shelf or slope environment at a few hundred meters
151 water depth, below storm wave base and probably oligophotic. The most common fossils
152 are large monaxon siliceous sponges spicules (up to 6 cm long), possibly of the class
153 Demospongea. Also abundant are conodonts of the genus *Mesogondolella,* which in the
154 Middle and Late Permian are indicative of cool-water environments, as inferred from their
155 boreal provincialism (Mei and Henderson 2001). The main species are *M. bitteri* and,
156 toward the top of the formation, *M. rosenkrantzi*, indicating a Capitanian age or, where *M.*
157 *rosenkrantzi* is found without *M. bitteri*, an early Wuchiapingian age (Henderson and Mei,
158 2007).

159 The upper contact of the RCF is defined by a major regional unconformity,
160 coinciding with the Guadalupian-Lopingian lowstand (Haq and Schutter, 2008). On the basis
161 of the conodont biostratigraphy, the duration of this unconformity has been estimated at 5-
162 7 million years. The Late Permian and Early Triassic are represented by the Phroso
163 Siltstone Member of the Sulphur Mountain Formation (SMF; Figs. 3-4), which is equivalent
164 to the Grayling Formation in northeastern British Columbia (Wignall and Newton, 2003).
165 The basal ~10 m of this unit represent a trangressive systems tract (TST) characterized by
166 an upward fining succession. Sediments consists of angular, immature silt to fine sand and
167 contains dolomite rhombs as well as reworked chert, micas, and microcrystalline carbonate.
168 Pyrite is also present, concentrated around organic fragments and, especially, in a cm-thick
169 bed that is ~10.5 cm above the basal unconformity. The lowermost beds of this unit are
170 bioturbated and contain abundant siliceous monaxon sponge spicules up to 2 cm in length,
171 but these features disappear abruptly ~40 cm above the basal unconformity. At the same
172 level, the conodont fauna dominated by *Mesogondolella* is abruptly replaced by a new fauna
173 dominated by the genus *Clarkina,* a transition that probably marks the latest Permian mass

extinction event (see below). Above this level, the SMF is composed of black to dark grey, pyritic, thin-bedded shale and siltstone. Benthic biota and bioturbation are lost, suggesting suboxic to anoxic bottom waters during deposition (Fig. 2) (Gibson, 1969, 1974; Gibson and Barclay, 1989; Henderson, 1997).

Four conodont biozones are present in the Sulphur Mountain Formation (Figs. 3-4), in ascending order:

1) *Mesogondolella sheni* Zone—Specimens of *M. sheni* from the basal TST of this formation indicate a Changhsingian age, but the exact relationship between these specimens and the type material from Selong, Tibet (Mei, 1996; Shen et al., 2006) remains uncertain. Specimens of *M. rosenkrantzi* and *M. bitteri* are considered to have been reworked from the underlying Ranger Canyon Formation during the transgression. The extent of reworking is difficult to address since all specimens are fragmented in these deformed shale units. At Ursula Creek in northeastern British Columbia, the uppermost Fantasque Formation contains both *M. sheni* and *M. rosenkrantzi*, indicating a Changhsingian age (Henderson, 1997; Wignall and Newton, 2003). We suggest a Late Changhsingian age for this assemblage at Opal Creek given that indisputably latest Changhsingian species are recovered only 40 cm higher in the section.

2) *Clarkina hauschkei–Clarkina meishanensis* Zone—This zone is defined by the association of *C. hauschkei*, *C. meishanensis*, *C. cf. changxingensis*, and *C. cf. zhejiangensis*. A comparable assemblage was recovered from the basal Blind Fiord Formation in the Canadian Arctic (Algeo et al., 2012). *C. hauschkei* is similar to specimens described as *C. hauschkei borealis* by Kozur (2005) from a zone immediately below the end-Permian microbialite facies at Abadeh, Iran. *C. meishanensis sensu stricto* is restricted to Beds 25 to 28 at Meishan (Jiang et al., 2007), but a similar species *C. zhangi* originally described as a

198 subspecies of *C. meishanensis* (Mei et al., 1998) ranges from Bed 23 to 24e at Meishan.
199 These two species may be synonymous and therefore range from Late Permian (Bed 23) to
200 Lower Triassic (Bed 28). Kozur (2005) indicated that *C. meishanensis* migrated into Iran
201 during the late Changhsingian, correlative with the Bed 23-24e interval at Meishan. At Opal
202 Creek, the base of this zone is marked by a sharp reduction in *Mesogondolella* (which
203 survives to the PTB) and the appearance of the genus *Clarkina*. The latter genus is typical of
204 the equatorial warm-water province during the Late Permian (Mei and Henderson, 2001),
205 and its appearance in the Canadian Western Sedimentary Basin is thus indicative of a
206 breakdown of a temperature barrier to migration (Henderson and Mei, 2007). The faunal
207 turnover at Opal Creek is either equivalent in age to, or slightly precedes that of, the main
208 extinction horizon (Bed 25) at Meishan, China (Jin et al., 2000).

209 3) *Hindeodus parvus–Clarkina taylorae* Zone—*H. parvus* is the key marker for the
210 base of the Triassic at the GSSP in Meishan, China (Yin et al., 1996, 2001); its occurrence
211 elsewhere does not define the PTB, but according to chronostratigraphic principles
212 indicates only proximity to it within the *H. parvus* Zone (Henderson, 2006). At Meishan and
213 elsewhere, the lowermost Triassic is typically characterized by a short-term acme of
214 *Hindeodus* (Chen et al., 2009; Jiang et al., 2007; Zhang et al., 2007). Although this genus is
215 rare at Opal Creek, some small, poorly preserved specimens were found in the lower ~6 m
216 of the SMF. The local first occurrence of *H. parvus* is ~1.5 m above the base of the SMF,
217 where it is found in association with *C. taylorae.* The latter taxon has not been recovered
218 with certainty below the PTB (Orchard et al., 1994), so the co-occurrence of these two
219 species is probably a good marker for the stratigraphic position of the PTB at Opal Creek.

220 4) *Clarkina taylorae–Clarkina cf. carinata* Zone—*C. carinata* (= *Neogondolella* of
221 some authors) is the most commonly identified Lower Triassic conodont species (Clark,

1959; Orchard and Krystyn, 1998; Sweet, 1970). The co-occurrence of *C. taylorae* and *C. cf. carinata* indicates a Griesbachian (Lower Induan) age.

3. Materials and methods

3.1. Field protocol

A total of 55 samples were collected over a 30-m-thick stratigraphic interval ranging from the Lower Permian Johnston Canyon Formation through the Lower Triassic Sulphur Mountain Formation for analysis of S isotopic compositions, S speciation, and trace-metal concentrations, with collection concentrated in the basal Sulphur Mountain Formation, around the extinction and boundary. An additional 14 samples were collected over a 1.4-m-thick stratigraphic interval at the base of the Sulphur Mountain Formation for analysis of Re-Os abundances and Os isotopic compositions. Samples were collected at 10 cm spacing from 20 cm above the Ranger Canyon/Sulphur Mountain unconformity to a level 1.6 m above the unconformity.

A separate set of 99 samples was collected at 40 cm intervals from the basal 44 m of the SMF, and processed at the University of Cincinnati. Carbon and sulfur elemental concentrations were determined using an Eltra 2000 C-S analyzer, and results calibrated using USGS and internal laboratory standards. Analytical precision was better than ±2.5% for carbon and ±5% for sulfur. An aliquot of each sample was digested in HCl at 50ºC for 12 hours, washed and filtered, and reanalyzed for C and S in order to determine concentrations of total organic carbon (TOC) and non-acid volatile sulfur (NAVS). These data are presented in Figure 5.

3.2. Sulfur isotopes

The ratio of sulfur stable isotopes ($^{34}S/^{32}S$) was measured by elemental analyzer continuous-flow isotope-ratio mass spectrometry (EA-CF-IRMS), at the University of Washington's IsoLab facility. Using a Eurovector EA and Thermo Finnigan Conflo III and MAT253 isotope-ratio mass spectrometer.

All stable isotope ratios for samples are reported in standard delta (δ) notation indicating the per mille (‰) difference from a standard:

$$\delta = (R_{sample}/R_{std}-1) \times 1000$$

where R equals $^{34}S/^{32}S$ of the standard or sample. The standard used for sulfur isotopes is Vienna Canyon Diablo Troilite (VCDT). The accuracy of ^{34}S measurements ($1\sigma = 0.2‰$, n = 20) was estimated through analysis of NIST NBS127 and NZ1 reference materials. Analytical precision (1σ) was determined based on replicates of an internal laboratory standard (Sigma Aldrich $BaSO_4$) during each run and was ≤0.2‰ (n = 5 to 10). The average precision (1σ) for sample duplicates was larger (0.6‰, n = 2-3), probably owing to sample heterogeneity.

Sulfur concentrations were also calculated for each sample by calibrating the total S signal for a range of masses of the internal standard during each isotopic analysis. In order to identify the relative contributions of different sulfur species (sulfates including carbonate associated sulfates, sulfides, organic sulfur, and barite) to total sulfur, different sample fractions were obtained by chemical processing. Sulfates were removed from sample aliquots by an acidification step, i.e., washing with an HCl solution (2N hydrochloric acid, 36-72 hours at 60°C), leaving only sulfide and organic S in the residue. An aliquot of the residue was then bleached, i.e., treated with a 5.5% NaClO solution (12-24h, 60°C) to

remove organic sulfur, leaving only the sulfide component, although some of the sulfide fraction may have been removed by this oxidation step. An aliquot of this second residue was then treated with a nitric acid wash (6N HNO_3, 24-48h, 60°C) in order to oxidize sulfides and isolate a possible barite component.

3.3. Re-Os isotopes

The Re-Os analytical protocol followed that described in detail by Selby and Creaser (2003) and Selby et al. (2007) and was carried out in the TOTAL Laboratory for Source Geochronology and Geochemistry at Durham University. Re was recovered by anion chromatography and further purified using single anion bead chromatography. The Re and Os isolates were analyzed for their isotopic compositions by negative thermal ionization mass spectrometry. The data presented here were analyzed in two separate batch analyses. Total procedural blanks for each batch were very similar, yielding [Re] = 15.1 and 17.2 pg/g, [Os] = 150 and 193 fg/g, $^{187}Os/^{188}Os$ of 0.21 and 0.19 for the first and second batches, respectively. In-house standard solutions of Re and Os were also run and were identical to the long-term running average reported in Rooney et al. (2010 and references therein).

3.4. Trace element concentrations

The chemical composition of the samples was measured by the ALS Chemex company of Vancouver, BC (Method ME-MS61). About 0.25 g of each sample was digested in perchloric, nitric, hydrofluoric and hydrochloric acids. The residue was suspended in dilute hydrochloric acid and analyzed by inductively coupled plasma-atomic emission spectrometry (ICP-AES). Samples containing high concentrations of bismuth, mercury, molybdenum, silver, or tungsten were diluted accordingly, then analyzed by inductively coupled plasma-mass spectrometry (ICP-MS). Results were corrected for spectral

interelemental interferences. Detection limits were 0.01% by mass for most major elements and <1 ppm for most trace elements.

To control for variations in sedimentation rate and terrigenous input, elemental data were normalized to aluminum (Al), which was used as a tracer for the aluminosilicate fraction of the sediment. For ease of comparison, elemental concentrations are reported as enrichment factors (EFs), which were calculated as:

$$EF_x = (\text{wt. \% X}/\text{wt. \% Al})_{sample} / (\text{wt. \% X}/\text{wt. \% Al})_{AUCC}$$

where X is the element in question and AUCC is Average Upper Continental Crust, as determined by McLennan (2001)

3.5. Petrographic analysis

Petrographic study of a subset of samples was undertaken at the University of Cincinnati and University of Kentucky. Standard petrographic thin sections were examined at 20-400X magnification under reflected light using a Leitz Laborlux 12-Pol optical microscope. Measurements were calibrated with a Zeiss micrometer. Polished sample chips were photographed under oil-immersion lenses at varying magnifications.

4. Results

4.1. Previous isotope results

Organic carbon and nitrogen isotope datasets were generated for the Ranger Canyon and Sulphur Mountain formations at the University of Washington's IsoLab facility. Both records showed significant excursions in the lowermost SMF, with a positive peak in $\delta^{13}C_{org.}$

315 and a negative shift in $\delta^{15}N$. These data were previously published in Schoepfer et al., 2012
316 with a full description of methods and supplementary data table; the data are shown here in
317 Figs. 3-4 for easy comparison with sulfur and trace element results.

318 *4.2. Sulfur speciation*

319 Average S concentrations of bulk samples (2.7±1.1%, n = 18) and acidified samples
320 (2.7±1.2%, n = 48) (omitting sample OC24, the pyrite bed) are nearly identical. In addition,
321 the difference between $\delta^{34}S$ for bulk and acidified extracts of the same samples is small
322 (0.8±1.0‰, n = 18). These observations suggest a negligible contribution of sulfates to the
323 total sulfur signal. All fully chemically processed (i.e., nitric-acid-treated) samples showed
324 sulfur levels below detection limits or too low (<0.03 wt%) to be significant, so little if any
325 barite is present. The bleaching step lowered sulfur levels significantly in all but one sample
326 (OC24, the pyrite bed), often to below detection limits. With such low S levels, $\delta^{34}S$ analysis
327 for bleached samples is much less precise, yet bleached $\delta^{34}S$ values are within +/- 5‰ of the
328 acidified-only $\delta^{34}S$ values, a much narrower spread than for the whole data set (> 30‰).
329 The relatively good agreement suggests the bleaching process was removing the majority of
330 a homogenous, labile sulfur pool that may be dominated by marcasite. This suggests the
331 acidified fraction represents an isotopically homogenous reduced sulfur pool ($S_{reduced}$, Fig. 3-
332 4), incorporating both sulfides and organic S.

333 [Insert Figure 3]

334 [Insert Figure 4]

335 *4.3. Sulfur concentration and isotopic profiles*

336 Sulfur isotopes vary markedly throughout the section, and several phases can be
337 distinguished (Figs. 3-4). In the Lower and Middle Permian, sediments are generally sulfur

poor (< 0.9 wt. %) and isotopically heavy, with $\delta^{34}S$ ranging from -5.4 to 7.2 ‰ (mean = 1.2 ‰, σ = 4.0), with the peak value 2.4 cm below the unconformity.

Heavy isotope values persist above the unconformity in the Late Permian lowermost SMF, despite much higher total sulfur content. A continuous and rapid decline in $\delta^{34}S$ can be observed between 1.5 and 29 cm (Fig. 4). This trend passes through the S wt. % maximum in the pyrite bed at ~10 cm, which has an S content of 26.4% by weight. Bleached extract for this sample yields S > 15wt% (IRMS signal saturated), and the S/Fe ratio is 1.13, nearly identical to the S/Fe ratios in pyrite (1.14), which along with field observation confirms that S in this layer is mostly in the form of pyrite. The declining isotope trend terminates in the section's $\delta^{34}S$ minimum at 29 cm ($\delta^{34}S$ = –32.0).

Above this minimum, sulfur concentrations and isotopes reach an equilibrium that they maintain for the remainder of the section. Sulfur weight % is generally at a few percent (mean = 2.3 %, σ = 1.0 %, Fig. 5) and $\delta^{34}S$ has a mean of -17.0‰ with a standard deviation of 6.0 ‰, though there is a gradual and poorly defined trend toward less negative values. There are also several minor positive excursions in $\delta^{34}S$. A small positive excursion in $\delta^{34}S$ (to –6 ‰) around 150 cm (sample OC145) is accompanied by a significant S concentration peak (6.3%).

[Insert Table 1]

[Insert Figure 5]

4.4. Petrographic data

Petrographic study revealed characteristic relationships between pyrite, organic matter, and calcite within the study samples. The basal beds (pre-LPME) of the SMF are characterized by high concentrations of sulfides in the form of massive pyrite (Fig. 6A) and large (5-50 μm), partially interlocking crystals of marcasite (Fig. 6B). These sulfides show

362 no relationship to primary sediment fabric; their quantity and form suggest that they may
363 be of hydrothermal original. The beds immediately above the LPME are characterized by
364 abundant pyrite framboids, although these framboids tend to be larger (5-10 μm; Fig. 6C)
365 than those formed in a euxinic water column (<5 μm; Wilkin et al., 1996; Wignall and
366 Newton, 1998). Many of the framboids show evidence of later diagenetic overgrowths (Fig.
367 6C-D), and blocky authigenic pyrite crystals are common (Fig. 6D-E). Higher in the section,
368 most pyrite occurs as clusters of framboidal or blocky crystals grown either within or on the
369 surface of large (50-500 μm) organic particles (e.g., Fig. 6G-H, L-N, P). Individual framboids
370 in these samples are often 10-40 μm in diameter (Fig. 6H, L, O) and hence distinctly larger
371 than syngenetic framboids (Wilkin et al., 1996). This form of pyrite is commonly associated
372 with large, blocky calcite crystals that have grown diagenetically within the sediment (e.g.,
373 Fig. 6G-J). Blocky to massive authigenic pyrite is sometimes found in the middle of large
374 carbonate-cemented areas without any obvious association with organic matter (e.g., Fig.
375 6F, K).

376 Several generations of carbonate are present in the sediments, including cements,
377 with isotopic measurements indicating a diagenetic origin (Schoepfer et al. 2012). This is
378 consistent with an increase in porewater alkalinity due to biological sulfate reduction and
379 the inference that most of pyrite in the section formed in the sediments after deposition.

380 [Insert Figure 6]

381 *4.5. Re-Os analysis*

382 The Re-Os data are presented in Table 2. Samples collected from 20 and 30 cm
383 above the Ranger Canyon/Sulphur Mountain unconformity are siltstone and did not contain
384 measureable Re and Os. Between 30 and 40 cm above the unconformity the siltstone grades
385 into black shale. The samples collected from this interval and to 1.6 m above the

386 unconformity are enriched in both Re and Os (~4 to 11 ppb; 78 to 157 ppt, respectively,
387 Table 2). The $^{187}Re/^{188}Os$ range between ~240 and 400, with the $^{187}Os/^{188}Os$ being
388 moderately radiogenic (~1.5 to 2.2). The initial $^{187}Os/^{188}Os$ (IOs) is calculated based on the
389 GTS 2008 age for the Permian-Triassic boundary, 252.2 Ma (Ogg et al., 2008; Shen S.Z. et al.,
390 2011) and the ^{187}Re decay constant of Smoliar et al. (1996). The calculated IOs values are
391 shown in Figure 4. Beginning 0.4 m above the unconformity (the LPME), the IOs values
392 become less radiogenic from 0.54 to 0.35. From the less radiogenic IOs at 0.6 m above the
393 unconformity to 1.5m (Permian-Triassic boundary) the IOs values become steadily more
394 radiogenic. At 1.6m the IOs trends to a less radiogenic value (~0.49).
395
396 [Insert Table 2]

397 *4.6. Trace-element redox proxies*

398 Certain trace elements tend to be authigenically enriched in sediments under
399 reducing conditions, including uranium (U), vanadium (V), and molybdenum (Mo) (Algeo
400 and Maynard, 2004; Tribovillard et al., 2006). The calculated Enrichment Factors of these
401 elements show similar patterns (Fig. 3), suggesting that they responded to a common redox
402 control. All three elements are highly enriched in the Johnston Canyon and Ranger Canyon
403 Formations, with Mo and U have EFs averaging >10x their concentrations in AUCC. These
404 values are probably indicative of sulfidic bottom water conditions throughout the
405 deposition of these units. All three elements show steep declines in the overlying SMF,
406 although varying somewhat in detail. V exhibits near-average values (EF ~1) throughout
407 the SMF. Mo and U remain modestly enriched (EF <10) in the SMF, with somewhat greater
408 enrichment in the basal 3 meters than higher in the formation. Relatively large EFs are
409 associated with the pyrite bed at ~10 cm, where Mo has an EF of 6.8 and U has an EF of 4.1.

As euxinic water conditions will often increase the particle reactivity of redox sensitive metals, which particularly often from organo-metallic compounds (Tribovillard et al., 2006), trace element concentrations were also normalized to TOC to control for the effects of particle flux. While the actual ratios varied greatly between elements, all were generally enriched in metals relative to TOC below the unconformity, but showed strong peaks in the lowermost Sulphur Mountain Formation coincident with the pyrite bed, and remained enriched throughout the latest Permian generally.

4.7. Trace-element productivity proxies

Several trace elements sensitive to changes in organic carbon export showed significant fluctuations throughout the section. Cu, Ni, Cd, Zn, Ba, and P all show a nutrient-like distribution in seawater and are mainly transferred to sediments through sinking carbon flux. Of these, Cu, Cd, Ni, and Zn can be precipitated as sulfide minerals under euxinic or sufficiently reducing conditions, and are likely to be preserved in sediments, whereas barium is generally precipitated as barite, a sulfate, and may be released back into the water column in a regime of sulfate reduction (Dehairs et al., 1980; Averyt and Paytan, 2004). Phosphorous is mainly stored in sediments in organic matter or phosphate minerals. Under reducing conditions, phosphate may be remineralized and re-enter the water column (Meyer and Kump, 2008).

EFs were calculated for Ba, P, Cu, Ni, Cd and Zn. These elements all showed significant enrichments above AUCC in the Johnston and Ranger Canyon Formations, with P in particular being enriched above AUCC by at least a factor of 7.9 and by 2 orders of magnitude in some samples. (2 samples collected 250 and 270 cm above the unconformity saturated the ICP-AES Phosphorous peak. The maximum detectable concentration, 10^4 ppm, was used). Directly above the unconformity, P remains highly enriched with an EF of

7.6 while Zn is also extremely enriched, with a EF of 77.4, likely due to precipitation as a sulfide in the pyrite bed. Cadmium, which also forms sulfide minerals, is also orders of magnitude more enriched in this layer than the rest of the section (EF=581.4). The other elements (Ba, Cu, Ni) drop off immediately above the unconformity to values similar to AUCC, with Ba and Cu generally below an EF of 1, whereas Ni remains just above. After the pyrite bed, Zn drops off to just below average EFs similar to Cu, Ni and Ba, while P remains slightly more enriched with EFs ranging from 1 to 2.6 through the remainder of the section. EFs are shown in logarithmic scale in Figure 3.

5. Discussion

5.1. Effects of sediment mixing on geochemical signals

Reworked conodonts above the unconformity indicate that some reworking of subaerially exposed Middle Permian cherts or biological mixing of sediments has occurred. This has the potential to exercise a controlling effect on geochemical signals, especially as the resemblance of the Late Permian lowermost Sulphur Mountain to the Middle Permian Ranger Canyon in many parameters (i.e. $\delta^{15}N$, $\delta^{34}S$, several trace elements) is central to interpretation of the outcrop.

While the lowermost Sulphur Mountain shows elevated EFs in several trace elements similar to or lower than the Ranger Canyon, this is after aluminum normalization, which obscures the often higher absolute concentrations of many elements in the more aluminosilicate rich Sulphur Mountain siltstones, for example the uppermost Ranger Canyon has a measured Zn content of 19 ppm, whereas the lowermost Sulphur Mountain has 3.85 ppt, In light of this orders of magnitude variation, it would be difficult for reworking or upward mixing of Ranger Canyon material to exercise any major control on

458 the trace element content above the unconformity. The presence of discrete peaks in
459 geochemical signals above the unconformity, for example the presence of an ~1 cm thick
460 pyrite bed, the positive organic carbon isotope excursion reported in Schoepfer et al. 2012,
461 Cd content, which spikes to 39.9 ppm at ~10 cm above the unconformity despite an average
462 of 0.3 ppm in the Ranger Canyon Formation suggests that mixing over decimeter scales is
463 not a controlling factor on the inorganic geochemistry of this interval.

464 The major isotopic shifts observed in the basal Sulphur Mountain, however, occur
465 over smaller spatial scales, and without an independent tracer, control by mixing cannot be
466 completely ruled out. If mixing is predominantly responsible for the heavy $\delta^{15}N$ and $\delta^{34}S$
467 values seen in the basal Sulphur Mountain, then the environmental changes implied by
468 these isotopic shifts may have occurred at any time during the missing 5-7 My Lopingian
469 interval, and may have occurred more gradually than the preserved isotope signals would
470 suggest, however it is worth noting that Luo et al. (2011) observed abrupt nitrogen isotope
471 shifts of similar magnitude immediately preceding the main LPME at several Tethyan
472 sections in South China.

473 *5.2. Benthic redox conditions*

474 Sulfur isotopic compositions provide information about the processes of sulfide
475 formation and, hence, paleomarine redox conditions. Syngenetic framboidal pyrite, which
476 forms in the water column and thus from an unlimited sulfate reservoir, commonly exhibits
477 a large negative fractionation relative to source sulfate (Goldhaber and Kaplan, 1974;
478 Canfield and Thamdrup, 1994). In contrast, authigenic pyrite formed in the sediment
479 exhibits heavier $\delta^{34}S$ values; if all porewater sulfate is consumed within a closed diagenetic
480 system, the resulting sulfide will have an average $\delta^{34}S$ value equal to that of the source
481 sulfate. The degree of shift toward heavier $\delta^{34}S$ values depends on the timing of bacterial

sulfate reduction (BSR); early BSR in a relatively open system will produce more ^{34}S-depleted sulfide than late BSR in a relatively closed system (Goldhaber and Kaplan, 1974; Chambers and Trudinger, 1979).

Modern seawater sulfate has a $\delta^{34}S$ of +20‰, yielding sulfide $\delta^{34}S$ values of about -30 to -40‰ in anoxic marine systems (Lyons, 1997; Wilkin and Arthur, 2001; Werne et al., 2003). The isotopic composition of seawater sulfate varied between +10‰ and +30‰ during the PTB transition, possibly shifting toward heavier values in the Early Triassic (Strauss, 1999; Newton and Wignall, 2004; Riccardi et al., 2006) although much variation exists within and between sections (Luo et al., 2010; Song et al., in review). Given a BSR fractionation of -30 to -60‰ (Habicht and Canfield, 2001), syngenetic pyrite in PTB sections should yield isotopic compositions between -10 and -40‰ (cf. Nielsen and Shen, 2004; Algeo et al., 2008).

Reduced sulfur $\delta^{34}S$ in the Johnston Canyon and Ranger Canyon formations average 1.0 ± 4.2‰ (n = 8). These relatively heavy values suggest precipitation in a closed system, consistent with a diagenetic origin for pyrite in this interval. The evidence of quantitative reduction of porewater sulfate in this interval despite the low organic content suggests poor postdepositional preservation may be responsible for the lack of preserved carbon despite other evidence of high productivity (see below).

The Johnston Canyon and Ranger Canyon formations contain high concentrations of V, U, and Mo. Coeval enrichments in Mo, U, and V (Fig. 3), suggest the presence of anoxic water in the Early and Middle Permian. That these enrichments are found in bioturbated sediments supporting an abundant (if homogenous) benthic fauna suggests that bottom water was oxygenated, and trace element enrichments may have resulted from a water column oxygen minimum impinging on the bottom. Coastal upwelling zones often

506 dynamically maintain an oxygen minimum zone (OMZ) in the mid-water column through
507 the decomposition of sinking organic material. When the sinking flux of carbon exceeds the
508 supply of oxygen, other electron acceptors are often used in decomposition, including
509 nitrate and sulfate, with upwelling zones being among the primary zones of denitrification
510 in the modern ocean (Seitzinger et al., 2006).

511 Nitrogen isotopes (Schoepfer et al. 2012) from Opal Creek suggest the Middle
512 Permian upwelling system supported a mid-water oxygen minimum where denitrification
513 and sulfate reduction were occurring. Denitrification has a substantial fractionation effect,
514 and when it does not occur quantitatively, enriches the residual marine nitrate pool. $\delta^{15}N$ in
515 the Ranger Canyon is consistently high, spiking to values above 9 ‰, values typically seen
516 in modern environments where denitrification occurs in a strong water column oxygen
517 minimum (Algeo et al. 2008).

518 The lower ~4 m of the SMF contains the largest concentrations of small framboids,
519 and these beds exhibit some of the most ^{34}S-depleted values—a pattern consistent with
520 pyrite mainly of syngenetic origin. $\delta^{34}S_{reduced}$ in the SMF averages -16.5 ± 6.8‰ (n = 47),
521 which is distinctly higher than the isotope compositions expected for syngenetic framboidal
522 pyrite. These compositions are consistent with pyrite formation in the diagenetic
523 environment under quasi-open conditions, or with diagenetic overgrowths on syngenetic
524 pyrite under somewhat more closed conditions.

525 TOC-S relationships are consistent with predominantly suboxic conditions during
526 deposition of the SMF. Most samples fall along the oxic-suboxic ("normal marine") trend of
527 Berner and Raiswell (1983; Fig. 5). A relative handful of samples, mostly in the lower ~4 m
528 of the SMF, exhibit S concentrations considerably above those expected for oxic-suboxic
529 facies; other evidence supports this interval having been deposited under primarily euxinic

conditions (see below). Three horizons higher in the SMF (at 4.7, 12.8, and 20.4 m) also exhibit significant S enrichment above the oxic-suboxic trendline (Fig. 5). Unlike samples from the base of the formation, however, these samples are associated with markedly heavier $\delta^{34}S$ values—an indication that the pyrite concentrations in these samples formed in the sediment and not in the water column, which is supported by petrographic data. The extinction of bioturbating benthic communities may have contribute to these intervals of near-quantitative sulfate reduction in the sediments (Shen Y. et al, 2011).

Secondary pyrite overgrowths are common in many framboidal layers, and framboid sizes are larger than those associated with syngenetic formation, especially above the basal 4 m of the SMF (Fig. 5). The observation that most framboids grew in clusters within or on the surface of large organic particles, rather than as isolated crystal aggregates, indicates a strong association of BSR with such organic substrates. The distribution of calcite within the samples, mostly as blocky diagenetic crystals adjacent to organic particles, or as "halos" enclosing these particles, is an indication that BSR within the sediment produced local increases in alkalinity that stimulated secondary carbonate precipitation (Berner, 1984).

Trace element proxies support these redox interpretations for the SMF. Mo, U, and V remain slightly enriched throughout the SMF, suggesting low oxygen conditions persisted, which along with the dearth of benthic biota, lack of bioturbation, and increased organic preservation indicate that the system transitioned to a bottom water oxygen minimum. Mo, which forms highly particle reactive oxythiomolybdates under euxinic conditions (Tribovillard et al., 2006), is particularly enriched in the lowermost 4 meters of the SMF, suggesting free sulfide in the water column during this interval.

553 Except for the basal ~50 cm of this formation, $\delta^{15}N$ is low and stable (Schoepfer et
554 al. 2012, Figs. 3-4), providing no evidence of water-column denitrification as might be
555 expected if suboxic conditions were due to high sinking fluxes of organic matter (e.g.,
556 Jenkyns et al., 2001; Algeo et al., 2008). Although the SMF consists predominantly of black
557 shale (Munsell color), TOC values are only moderate (0.2-3.0%) yet locally higher than
558 expected for oxic-suboxic facies (Algeo and Maynard, 2004). One explanation for this
559 pattern may be a marked reduction in bioturbation intensity during the Early Triassic, as a
560 consequence of the loss of most benthic infauna during the LPME (Twitchett and Wignall,
561 1996) and transition from a mid-water to bottom water oxygen minimum. Reduced
562 bioturbation would severely constrain ventilation of the sediment and allow greater
563 quantities of organic matter to be preserved for a given flux of organic matter to the
564 sediment-water interface. Thus, multiple lines of evidence confirm that the basal ~4 m of
565 the SMF coincided with a euxinic event, and that the remainder of the formation was
566 deposited under oxic to suboxic conditions.

567

568 *5.3. Marine circulation and productivity*

569

570 The consistent enrichments in Ba, Cu, Ni, Zn, P, and Cd in the Johnson Canyon and
571 Ranger Canyon formations are here interpreted as representing a highly productive,
572 eutrophic marine system, despite the generally low organic carbon content of these units,
573 which may results from poor preservation in well-ventilated bottom water. The presence of
574 phosphate nodules in the Johnson Canyon and minor phosphatic material in the Ranger
575 Canyon is consistent with a high-productivity environment, and the dominant fauna of the
576 Ranger Canyon, rock-forming abundances of filter-feeding sponges, suggests a vigorous
577 export of organic detritus from the photic zone.

High-abundance but low-diversity conodont assemblages have been suggested to indicate eutrophic conditions (Brasier, 1995), because fast-breeding species capable of rapidly exploiting the available resources tend to dominate the environment. The conodont assemblage of the Ranger Canyon Formation is dominated by high abundances of the genus *Mesogondolella*, which had a circumboreal distribution in the Middle Permian and is therefore also indicative of cold-water conditions (Henderson, 1997; Mei and Henderson, 2001).

The biota of the Johnston Canyon and Ranger Canyon formations is consistent with a high-nutrient, cold-water environment. Replacement of this prolific carbonate factory by a siliceous sponge-dominated biota occurred between the Artinskian (late Early Permian) and Guadalupian (late Middle Permian) as a consequence of climatic cooling and an increase in nutrient levels (Beauchamp and Henderson, 1994; Reid et al., 2007; Bensing et al., 2008). The high concentration of sponge-derived chert in Upper Permian beds has been interpreted as evidence of vigorous thermohaline circulation and nutrient upwelling in the Panthalassic Ocean, and its absence in Lower Triassic beds as evidence of sluggish circulation and nutrient-poor surface waters (Beauchamp, 1994; Beauchamp and Desrochers, 1997; Beauchamp and Baud, 2002). Hyalosponge facies, indicative of cold, deepwater conditions, are widespread along the western margin of Pangaea during the Early to Middle Permian, and have been used to infer the presence of coastal upwelling down to subtropical latitudes, as well as cold northern polar currents driven by sea ice in contact with the ocean (Beauchamp and Baud, 2002). Upwelling at subtropical latitudes along western Pangaea is also inferred by Ziegler et al. (1998) from sedimentological evidence, and has been modeled under a range of atmospheric conditions by Winguth and Maier-Reimer (2005).

The locality was erosive throughout most of the Lopinigian lowstand, but when

603 sedimentation resumed in the Changshingian the depositional environment resembled that
604 of the Ranger Canyon in many ways. Silica sponges were still the abundant, predominant
605 benthic fauna, although sponge spicules were increasingly diluted with siliciclastic
606 sediments. Nitrogen and sulfur isotopes remain highly enriched, suggesting that an anoxic
607 zone, fed by sinking organic matter and ultimately by upwelling nutrients, persisted into the
608 latest Permian. Sediments remain bioturbated in this interval, indicating that the sea floor
609 was relatively well oxygenated, with the oxygen minimum occurring in the water column.

610 ~ 10 cm above the unconformity is a continuous bed containing >26% sulfur by
611 weight, mostly in the form of pyrite, suggestive of highly euxinic water conditions, which is
612 supported by orders-of-magnitude enrichments in the S/TOC and Mo/TOC ratios. This ~1
613 cm thick pyrite bed corresponds with a discrete, ~ 8 ‰ spike in organic carbon isotopes
614 that has been interpreted as transient increase in productivity (Schoepfer et al. 2012) which
615 may have driven the system toward euxinia, Enrichments in P, Zn, and Cd are also
616 suggestive of enhanced productivity in this interval: while Zn and Cd are expected to
617 complex in the sulfide sediments, P should be unaffected by euxinia and record
618 productivity, whereas minor depletions in Barium relative to AUCC may reflect the difficulty
619 of preserving barite ($BaSO_4$) under conditions of euxinia.

620 The trace element enrichments suggest that this euxinic interval may have been
621 fueled by transient increased productivity. Numerous workers have suggested a substantial
622 increase in continental weathering and erosion in the latest Permian (Ward et al. 2000;
623 Sephton et al., 2005; Algeo and Twitchett, 2010; Algeo et al., 2011). This would have carried
624 an increased complement of terrigenous nutrients, such as phosphate and iron, and may
625 have pushed organic productivity above its already-high levels, driving the system toward
626 euxinia.

627 This hypothesis receives some support from the *I*Os data (Fig. 4). The primary
628 feature of this data set is a shift from relatively non-radiogenic values (0.35-0.40) around
629 the LPME boundary toward more radiogenic values (~0.45 to 0.62) between 60 and 150 cm
630 above the unconformity. This suggests that the primarily control of the Os composition in
631 seawater during this interval (Os_{SW}) is the influx of radiogenic detritus from the cratonic
632 continental crust (Cohen et al., 1999; Peucker-Ehrenbrink and Ravizza, 2000), into the
633 ocean, beginning roughly with the onset of the euxinic pulse. Unradiogenic Os values seen
634 prior to this shift may be related to the input of Os associated with the eruption of the
635 Siberian Traps, which would be expected to possess mantle-like Os isotope signatures
636 (~0.13-0.15; Horan et al., 1995). Values for Os_{SW} during the late Permian Arctic black shale
637 of the Mid-Norwegian shelf yield *I*Os values of ~0.6 (Georgiev et al., 2011), which is similar
638 to the *I*Os value of the extinction interval (~0.55) at Opal Creek, suggesting these
639 continental weathering effects may have been widespread in the global ocean. However, in
640 stark contrast to the Arctic black shales the $^{187}Re/^{188}Os$ values of the Opal Creek P-T section
641 are typical of most marine organic-rich sedimentary rocks (269-394; Table 2) and therefore
642 indicate that the conditions that permitted elevated $^{187}Re/^{188}Os$ values (~2000 to 6000) in
643 the Arctic is regional rather than global as suggested by Georgiev et al. (2011).

644 The end of this intensely euxinic interval corresponds with a drop off in the
645 previously enriched isotopes of nitrogen and sulfur. Nitrogen isotopes fall toward low
646 values of approximately 2-3 ‰, lower than average modern marine nitrate and likely
647 reflecting the influence of nitrogen fixation from the atmosphere in a nutrient limited
648 environment. These low nitrogen values persist with remarkable uniformity throughout the
649 remainder of the SMF, reflecting a new nutrient cycling regime in which water
650 denitrification, fueled by respiration of sinking organic matter, no longer occurred on a
651 significant scale. These changes probably reflect the collapse of vigorous coastal upwelling

652 and the concomitant high organic productivity that fueled anaerobic respiration in the
653 water column.

654 This is supported by the collapse of all productivity-sensitive trace elements to values
655 very near AUCC throughout the remainder of the section (excepting P and Cd, which remain
656 slightly enriched), and by the disappearance of silica-producing sponges 30 cm above the
657 pyrite bed, in what we interpret as corresponding to the main Permian-Triassic marine
658 extinction. Productivity in the subsequent SMF likely reflected typical values for
659 oligotrophic marine settings, rather than those of continental margin upwelling systems,
660 and may have been limited by nitrogen availability, with diazotrophic prokaryotes likely
661 playing an important role. The cessation of upwelling may have been the result of warming
662 following the eruption of the Siberian traps, with a consequent flattening of global thermal
663 gradients and slowing of ocean and atmospheric circulation, with both euxinia and
664 increasing nutrient limitation playing a role in bringing about benthic extinctions in this
665 ecosystem.

666

667 *5.4. Integrated model*

668

669 Here we present evidence that a coastal upwelling system, a major mode of
670 Panthalassic ocean circulation that had persisted for tens of millions of years, abruptly
671 terminated preceding the Permian-Triassic boundary, shifting to a relatively unproductive,
672 nutrient limited system with suboxic to dysoxic bottom water. However, this transition was
673 preceded by an interval of intense euxinia, corresponding to the pyrite bed and preceding
674 the main pulse of marine extinction. This likely resulted from a transient intensification of
675 marine productity, which may have been caused by a combination of warming climate with
676 residual upwelling of nutrient rich waters, before the circulation slowed dramatically (Fig.

7). Higher temperatures could allow for faster algal growth and nutrient cycling, and ultimately faster and more explosive productivity. Alternatively, this pulse of high productivity may have been a global ocean scale event. The end-Permian has been linked to a change in fluvial morphology patterns, and a die off of vegetation combined with a warmer and more acidic hydrosphere following the eruption of the Siberian traps may have led to faster continental weathering and increased nutrient input into the oceans. The immaturity of siliciclastic sediments in the lowermost Sulphur Mountain Formation suggest rapid weathering was occurring. Thin pyrite beds have been found in latest Permian marine sediments along western Pangaea up into the Canadian arctic (Grasby and Beauchamp, 2009). Increased nutrient inputs may have led to one or several pulses of high productivity in latest Permian coastal oceans, driving environments to extinction-causing levels of anoxia and euxinia despite the long-term trend toward slower circulation and nutrient cycling into the Triassic.

[Insert Figure 7]

6. Conclusions

The Permian at Opal Creek records an active cold-water coastal upwelling zone that supported high productivity and a mid-water oxygen minimum zone where anaerobic respiration occurred. This system persisted for tens of millions of years only to abruptly terminate preceding the end-Permian extinction. Despite the Panthalassic Ocean's potentially dominant role in Permian biogeochemical cycling, there have been few ways to test the impact of the end-Permian crisis on circulation and ventilation. Here we present

isotopic and trace element evidence for the cessation of coastal upwelling, a modality of oceanic circulation that leaves distinctive isotopic signatures. Despite the apparent slowdown of circulation at the end Permian, a major, discrete euxinic pulse preceded the extinction, and corresponds to a number of geochemical indicators of high productivity. A transient pulse of increased carbon export may have been necessary to drive coastal oceans toward the euxinia necessary for mass extinction.

Acknowledgments

The authors would like to acknowledge the generous support provided by The United States National Science Foundation (NSF) and NASA Astrobiology Institute (NAI) University of Washington node as well as the Natural Sciences and Engineering Research Council (NSERC) of Canada, and the University of Washington Earth and Space Sciences Department. Our gratitude goes out to the staff of the University of Washington IsoLab facility for their extensive help with our isotopic analyses. TJA thanks the National Science Foundation for support (EAR-0618003, EAR-0745574, and EAR-1053449). YS would like to thank the National Natural Science Foundation of China for their support (41025011).

721 **References**

722

723 Algeo, T.J., Maynard, J.B., 2004. Trace element behavior and redox facies in core shales of
724 Upper Pennsylvanian Kansas-type cyclothems. Chemical Geology 206, 289-318.

725 Algeo, T.J., Chen, Z.Q., Fraiser, M.L., Twitchett, R.J., 2011a. Terrestrial-marine teleconnections
726 in the collapse and rebuilding of Early Triassic marine ecosystems. Palaeogeography,
727 Palaeoclimatology, Palaeoecology 308, 1-11.

728 Algeo, T., Henderson, C., Ellwood, B., Rowe, H., Elswick, E., Bates, S., Lyons, T., Hower, J.C.,
729 Smith, C., Maynard, J.B., Hays, L., Summons, R., Fulton, J., Freeman, K., 2012. Evidence
730 for a diachronous Late Permian marine crisis from the Canadian Arctic region.
731 Geological Society of America Bulletin, in press.

732 Algeo, T.J., Hinnov, L., Moser, J., Maynard, J.B., Elswick, E., Kuwahara, K., Sano, H., 2010.
733 Changes in productivity and redox conditions in the Panthalassic Ocean during the
734 latest Permian. Geology 38, 187-190; doi:10.1130/G30483.1.

735 Algeo, T.J., Kuwahara, K., Sano, H., Bates, S., Lyons, T., Elswick, E., Hinnov, L., Ellwood, B.,
736 Moser, J., Maynard, J.B., 2011b. Spatial variation in sediment fluxes, redox conditions,
737 and productivity in the Permian-Triassic Panthalassic Ocean, Palaeogeography,
738 Palaeoclimatology, Palaeoecology 308, 65-83 doi: 10.1016/j.palaeo.2010.07.007

739 Algeo, T., Rowe, H., Hower, J.C., Schwark, L., Herrmann, A., Heckel, P., 2008. Changes in ocean
740 denitrification during Late Carboniferous glacial-interglacial cycles. Nature Geoscience
741 1, 709-714; doi:10.1038/ngeo307.

742 Algeo, T.J., Shen, Y., Zhang, T., Lyons, T., Bates, S., Rowe, H., Nguyen, T.K.T., 2008. Association
743 of ^{34}S-depleted pyrite layers with negative carbonate $\delta^{13}C$ excursions at the Permian-

744 Triassic boundary: Evidence for upwelling of sulfidic deep-ocean water masses.
745 Geochemistry Geophysics Geosystems 9, Q04025, 10 pp.

746 Algeo, T.J., and Twitchett, R.J., 2010. Anomalous Early Triassic sediment fluxes due to
747 elevated weathering rates and their biological consequences. Geology 38, 1023-1026.
748
749 Algeo, T.J., Wilkinson, B.H., Lohmann, K.C, 1992. Meteoric-burial diagenesis of
750 Pennsylvanian carbonate: water/rock interactions and basin geothermics. Journal of
751 Sedimentary Petrology 62, 652-670.

752 Averyt, K.B., Paytan, A., 2004. A comparison of multiple proxies for export production in the
753 equatorial Pacific. Paleoceanography 19, PA4003, 14 pp.

754 Baublys, K. A., Golding, S. D., Young, E. and Kamber, B. S. (2004), Simultaneous
755 determination of $\delta^{33}S_{V\text{-}CDT}$ and $\delta^{34}S_{V\text{-}CDT}$ using masses 48, 49 and 50 on a continuous
756 flow isotope ratio mass spectrometer. Rapid Communications in Mass Spectrometry,
757 18: 2765–2769

758 Baud, A., Magaritz, M., Holser, W.T., 1989. Permian–Triassic of the Tethys: carbon isotope
759 studies. Geologische Rundschau 78, 649–677.

760 Beauchamp, B., 1994. Permian climatic cooling in the Canadian Arctic, in Klein, G.D., ed.,
761 Pangea: Paleoclimate, Tectonics and Sedimentation during Accretion, Zenith and
762 Break-up of a Super-Continent. Geological Society of America Special Paper 288, pp.
763 229-246.

764 Beauchamp, B., Baud, A., 2002. Growth and demise of Permian biogenic chert along
765 northwest Pangea: evidence for end-Permian collapse of thermohaline circulation.
766 Palaeogeography, Palaeoclimatology, Palaeoecology 184, 37-63.

767 Beauchamp, B., Desrochers, A., 1997. Permian warm- to very cold carbonates and cherts in
768 northwest Pangea. In: James, N.P., Clarke, J. (eds.), Cool Water Carbonates. Society of
769 Economic Geologists and Paleontologists Special Publication 56, pp. 327-347.

770 Beauchamp, B., Henderson, C.M., 1994. The Lower Permian (Artinskian) Raanes, Great Bear
771 Cape, and Trappers Cove formations, Sverdrup Basin, Canadian Arctic: Stratigraphy
772 and conodont zonation. Bulletin of Canadian Petroleum Geology 42, 565-600.

773 Beauchamp, B., Henderson, C.M., Grasby, S.E., Gates, L.T., Beatty, T.W., Utting, J., James, N.P.
774 2009. Late Permian sedimentation in the Sverdrup Basin, Canadian Arctic: the
775 Lindström and Black Stripe Formations. Bulletin of Canadian Petroleum Geology 57,
776 167-191.

777 Becker, L., Poreda, R.J., Hunt, A.G., Bunch, T.E., Rampino, M. 2001. Impact event at the
778 Permian-Triassic boundary: evidence from extraterrestrial noble gases in fullerenes.
779 Science 291, 1530-1533.

780 Bensing, J.P., James, N.P., Beauchamp, B., 2008. Carbonate deposition during a time of mid-
781 latitude ocean cooling: Early Permian "subtropical" sedimentation in the Sverdrup
782 Basin, Arctic Canada. Journal of Sedimentary Research 78, 2-15.

783 Benton, M.J., Tverdokhlebov, V.P, Surkov, M.V., 2004. Ecosystem remodeling among
784 vertebrates at the Permian-Triassic boundary in Russia. Nature 432, 97-100.

785 Benton, M.J., Twitchett, R.J., 2003. How to kill (almost) all life: the end-Permian extinction
786 event. Trends in Ecology and Evolution, 18 No.7 July 2003.

787 Berner, R.A., 1984. Sedimentary pyrite formation: an update. Geochimica et Cosmochimica
788 Acta 48, 605-615.

789 Berner, R.A., 2002. Examination of hypotheses for the Permo-Triassic boundary extinction
790 by carbon cycle modeling. Proceedings of the National Academy of Sciences (U.S.A.) 99,
791 4172-4177.

792 Berner, R.A., Kothavala, Z., 2001. GEOCARB III: a revised model of atmospheric CO_2 over
793 Phanerozoic time. American Journal of Science 301, 182-204.

794 Berner, R.A., Raiswell, R., 1983. Burial of organic carbon and pyrite sulfur in sediments over
795 Phanerozoic time: a new theory. Geochimica et Cosmochimica Acta 47, 855-862.

796 Bottjer, D.J., Clapham, M.E., Frasier, M.L., Powers, C.M., 2008. Understanding mechanisms for
797 the end-Permian mass extinction and the protracted Early Triassic aftermath and
798 recovery. GSA Today 18, 4-10.

799 Brasier, M.D., 1995. Fossil indicators of nutrient levels, 1. Eutrophication and climate
800 change. Geological Society of London Special Publications 83, pp. 113-132.

801 Brookfield, M.E., Twitchett, R.J., Goodings, C., 2003. Palaeoenvironments of the Permian
802 Triassic transition sections in Kashmir, India. Palaeogeography, Palaeoclimatology,
803 Palaeoecology 198, 353-371.

804 Canfield, D.E., Thamdrup, B., 1994. The production of ^{34}S-depleted sulfide during bacterial
805 disproportionation of elemental sulfur. Science 266, 1973-1975

806 Chambers, L.A., Trudinger, P.A., 1979. Microbiological fractionation of stable sulfur isotopes:
807 A review and critique. Geomicrobiological Journal 1, 249-293.

808 Chen, J., Beatty, T.W., Henderson, C.M., Rowe, H., 2009. Conodont biostratigraphy across the
809 Permian-Triassic boundary at the Dawen section, Great Bank of Guizhou, Guizhou
810 Province, South China: Implications for the Late Permian extinction and correlation
811 with Meishan. Journal of Asian Earth Sciences 36, 442-458.

812 Clark, D.L., 1959. Conodonts from the Triassic of Nevada and Utah. Journal of Paleontology
813 33, 305-312.
814 Cohen, A. S., Coe, A. L., Bartlett, J. M., Hawkesworth, C. J., 1999: Precise Re-Os ages of organic-
815 rich mudrocks and the Os isotope composition of Jurassic seawater. Earth and
816 Planetary Science Letters 167, 159-173.
817 Dehairs, F., Chesselet, R., Jedwab, J., 1980. Discrete suspended particles of barite and the
818 barium cycle in the open ocean. Earth and Planetary Science Letters 49, 528-550.
819 Erwin, D.H., Bowring, S.A., Jin, Y.-G., 2002. End-Permian mass-extinctions: A review. In:
820 Koeberl, C., MacLeod, K.G. (Eds.), Catastrophic Events and Mass Extinctions: Impacts
821 and Beyond. Geological Society of America Special Paper 356, pp. 353-383.
822 Fraiser, M.L., Bottjer, D.J., 2007. Elevated atmospheric CO_2 and the delayed biotic recovery
823 from the end-Permian mass extinction. Palaeogeography, Palaeoclimatology,
824 Palaeoecology 252, 164-175.
825 Fry, B., Silva, S. R., Kendall, C., Anderson, R. K. (2002), Oxygen isotope corrections for online
826 $\delta^{34}S$ analysis. Rapid Communications in Mass Spectrometry, 16: 854–858
827 Gates, L.M., James, N.P., Beauchamp, B., 2004. A glass ramp: Shallow-water Permian
828 spiculitic chert sedimentation, Sverdrup Basin, Arctic Canada. Sedimentary Geology
829 168, 125-147.
830 Georgiev, S., Stein, H.J., Hannah, J.L., Bingen, B., Weiss, H.M., Piasecki, S. 2011. Hot acidic Late
831 Permian seas stifle life in record time. Earth and Planetary Science Letters 310, 389-
832 400.
833 Gibson, D.W., 1969. Triassic stratigraphy of the Bow River-Crowsnest Pass region, Rocky
834 Mountains of Alberta and British Columbia. Geological Survey of Canada, Paper 68, 29,
835 48.

836 Gibson, D.W., 1974. Triassic rocks of the Southern Canadian Rocky Mountains. Geological
837 Survey of Canada, Bulletin 230, 65.

838 Gibson, D.W., Barclay, J.E., 1989. Middle Absaroka Sequence, The Triassic Stable Craton. In:
839 Ricketts, B. (ed.) Basin Analysis --The Western Canada Sedimentary Basin, Canadian
840 Society of Petroleum Geologists Special Publication, pp. 219-231.

841 Goldhaber, M.B., Kaplan I.R., 1974. The sulfur cycle. In: Goldberg, E.D. (ed.), The Sea, vol. 5.
842 Wiley, pp. 569-655.

843 Grasby, S.E., Beauchamp, B., 2009. Latest Permian to Early Triassic basin-to-shelf anoxia in
844 the Sverdrup Basin, Arctic Canada. Chemical Geology 264, 232-246.

845 Grice, K., Cao, C., Love, G.D., Bottcher, M.E., Twitchett, R.J., Grosjean, E., Summons, R.E.,
846 Turgeon, S.C., Dunning, W., Jin, Y., 2005. Photic zone euxinia during the Permian-
847 Triassic superanoxic event. Science 307, 706-709.

848 Habicht, K.S., Canfield, D.E., 2001. Isotope fractionation by sulfate-reducing natural
849 populations and the isotopic composition of sulfide in marine sediments. Geology 29,
850 555-558.

851 Haq, B.U., Schutter, S.R., 2008. A chronology of Paleozoic sea-level changes. Science 322, 64–
852 68.

853 Hays, L.E., Beatty, T., Henderson, C.M., Love, G.D., Summons, R.E., 2007. Evidence for photic
854 zone euxinia through the end-Permian mass extinction in the Panthalassic Ocean
855 (Peace River Basin, Western Canada). Palaeoworld 16, 39-50.

856 Henderson, C.M., 1989. Absaroka Sequence - The Lower Absaroka Sequence: Upper
857 Carboniferous and Permian (Chapter 10). In: Ricketts, B. (ed.) Basin Analysis - The
858 Western Canada Sedimentary Basin, Canadian Society of Petroleum Geologists Special

Publication, pp. 203-217.

Henderson, C.M., 1997. Uppermost Permian conodonts and the Permian-Triassic boundary in the Western Canada Sedimentary Basin. Bulletin of Canadian Petroleum Geology 45, 693-707.

Henderson, C.M., Baud, A., 1997. Correlation of the Permian-Triassic boundary in Arctic Canada and comparison with Meishan, China, in Proceedings of the 30th International Geological Congress, v. 11, VSP Scientific Publishers, pp. 143-152.

Henderson, C.M., 2006. Beware of your FO and be aware of the FAD. Permophiles 47, 8-9.

Henderson, C.M., Mei, S., 2007. Geographical clines in Permian and Lower Triassic gondolellids and its role in taxonomy. Palaeoworld 16, 190-201.

Henderson, C.M., Richards, B.C., Barclay, J.E., 1994. Permian. In: Mossop, G.D. (ed.) Geological Atlas of the Western Canada Sedimentary Basin Joint publication of the Canadian Society of Petroleum Geologists and the Alberta Research Council, pp. 251-258.

Horan, M.F., Walker, R.J., Fedorenko, V.A., Czamanske, G.K. 1995. Osmium and neodymium isotopic constraints on the temporal and spatial evolution of Siberian flood basalt sources. Geochimica et Cosmochimica Acta 59, 5159–5168

Hotinski, R.M., Bice, K.L., Kump, L.R., Najjar, R.G., Arthur, M.A., 2001. Ocean stagnation and end-Permian anoxia. Geology 29, 7-10.

Huey, R.B., Ward, P.D., 2005. Hypoxia, global warming, and terrestrial Late Permian extinctions. Science 308, 398-401.

Hunt, J.M., 1996. Petroleum Geochemistry and Geology, 2nd ed., W.H. Freeman, New York, 743 pp.

Isozaki, Y., 1994. Superanoxia across the Permo–Triassic boundary: record in accreted

882 deep-sea pelagic chert in Japan. In: Embry, A.F., Beauchamp, B., Glass, D.J. (eds.),
883 Pangea: Global Environments and Resources. Canadian Society of Petroleum Geologists,
884 Memoir, vol. 17, pp. 805–812.

885 Isozaki, Y., 1997. Permo-Triassic boundary superanoxia and stratified superocean: records
886 from lost deep-sea. Science 276, 235-238.

887 Isozaki, Y., Kawahata, H., Ota, A., 2007. A unique carbon isotope record across the
888 Guadalupian-Lopingian (Middle-Upper Permian) boundary in mid-oceanic paleo-atoll
889 carbonates: The high-productivity "Kamura event" and its collapse in Panthalassa.
890 Global and Planetary Change 55, 21-38.

891 Jenkyns, H.C., Gröcke, D.R., Hesselbo, S.P., 2001. Nitrogen isotope evidence for water mass
892 denitrification during the early Toarcian (Jurassic) oceanic anoxic event.
893 Paleoceanography 16, 593-603.

894 Jiang, H., Lai, X., Luo, G., Aldridge, R., Zhang, K., Wignall, P., 2007. Restudy of conodont
895 zonation and evolution across the P/T boundary at Meishan section, Changxing,
896 Zhejiang, China. Global and Planetary Change 55, 39-55.

897 Jin, Y.G., Wang, Y., Wang, W., Shang, Q.H., Cao, C.Q., Erwin, D.H., 2000. Pattern of marine mass
898 extinction near the Permian Triassic boundary in South China. Science 289, 432-436.

899 Kashiyama Y., Ogawa, N.O., Kuroda, J., Shiro M., Nomoto S., Tada R., Kitazato H., Ohkouchi N.,
900 2008. Diazotrophic cyanobacteria as the major photoautotrophs during mid-
901 Cretaceous oceanic anoxic events: Nitrogen and carbon isotopic evidence from
902 sedimentary porphyrin. Organic Geochemistry 39, 532-549.

903 Kidder, D.L., Worsley, T.R., 2003. Late Permian warming, the rapid latest Permian
904 transgression, and the Permo-Triassic extinction, 2003 GSA Annual Meeting: Seattle,

905 WA.

906 Kidder, D.L., Worsley, T.R., 2004. Causes and consequences of extreme Permo-Triassic
907 warming to globally equable climate and relation to the Permo-Triassic extinction and
908 recovery. Palaeogeography, Palaeoclimatology, Palaeoecology 203, 207-237.

909 Kiehl, J.T., Shields, C.A., 2005. Climate simulation of the latest Permian: implications for mass
910 extinction. Geology 33, 757-760.

911 Kim, S.T., O'Neil, J. R.. 1997. Equilibrium and nonequilibrium oxygen isotope effects in
912 synthetic carbonates. Geochimica et Cosmochimica Acta 61, 3461-3475.

913 Knoll, A.H., Bambach, R.K., Canfield, D.E., Grotzinger, J.P., 1996. Comparative Earth history
914 and Late Permian mass extinction. Science 273, 452-457.

915 Korte, C., Kozur, H.W., 2010. Carbon-isotope stratigraphy across the Permian-Triassic
916 boundary: A review. Journal of Asian Earth Sciences, doi:10.1016/j.jseaes.2010.01.005

917 Korte, C., Pande, P., Kalia, P., Kozur, H.W., Joachimski, M., Oberhänsli. H., 2010. Massive
918 volcanism at the Permian–Triassic boundary and its impact on the isotopic
919 composition of the ocean and atmosphere. Journal of Asian Earth Sciences 37, 293-311.

920 Kozur, H.W., 2005. Pelagic uppermost Permian and Permian-Triassic boundary conodonts
921 of Iran. Part II: investigated sections and evaluation of the conodont faunas. Hallesches
922 Jahrbuch Fur Geowissenschaften, Reihe B: Geologie, Palaontologie, Mineralogie, 19, 49-
923 86.

924 Krull, E.S., Retallack, G.J., Campbell, H.J., Lyon, G.L.., 2000. $\delta^{13}C_{org}$ chemostratigraphy of the
925 Permian-Triassic boundary in the Maitai Group, New Zealand: Evidence for high-
926 latitudinal methane release. New Zealand Journal of Geology and Geophysics 43, 21-32.

927 Kump, L.R., Pavlov, A., Arthur, M.A., 2005. Massive release of hydrogen sulfide to the surface
928 ocean and atmosphere during interval of oceanic anoxia. Geology 33, 397-400.

929 Looy, C.V., Twitchett, R.J., Dilcher, D.L., van Konijnenburg-van Cittert, J.H.A., Visscher, H.,
930 2001. Life in the end-Permian dead zone. Proceedings of the National Academy of
931 Sciences (U.S.A.) 98, 7879-7883.

932 Luo, G., Kump, L.R., Wang, Y., Tong, J., Arthur, M.A., Yang, H., Huang, J., Yin, H., Xie, S., 2010.
933 Isotopic evidence for an anomalously low oceanic sulfate concentration following end-
934 Permian mass extinction. Earth and Planetary Science Letters 300, 101-111.

935 Luo, G., Wang, Y., Kump, L.R., Bai, X., Algeo, T.J., Yang, H., Xie, S., 2011. Nitrogen fixation
936 prevailed simultaneously with the end-Permian marine mass extinction and its
937 implications. Geology, v. 39, p. 647-650.

938 Luo, G., Wang, Y., Yang, H., Algeo, T.J., Kump L.R., Huang, J., Xie, S., 2011. Stepwise and large-
939 magnitude negative shift in $\delta^{13}C_{carb}$ preceded the main marine mass extinction of the
940 Permian-Triassic crisis interval. Palaeogeography, Palaeoclimatology, Palaeoecology
941 299, 70-82.

942 Lyons, T.W., 1997. Sulfur isotopic trends and pathways of iron sulfide formation in upper
943 Holocene sediments of the anoxic Black Sea. Geochimica et Cosmochimica Acta 61,
944 3367-3382.

945 McLennan, S.M., 2001. Relationships between the trace element composition of sedimentary
946 rocks and upper continental crust. Geochemistry Geophysics Geosystems, 2, GC000109,
947 24 pp.

948 Mei, S., 1996. Restudy of conodonts from the Permian-Triassic boundary beds at Selong and
949 Meishan and the natural Permian-Triassic boundary. In: Wang, H. and Wang, X. (eds.).

950 Memorial Volume of Prof. Sun Yunzhu: Palaeontology and Stratigraphy. Centennial
951 China University of Geosciences Press, Wuhan, pp. 141-148.

952 Mei, S., Henderson, C.M. 2001. Evolution of Permian conodont provincialism and its
953 significance in global correlation and paleoclimatic implication. Palaeogeography,
954 Palaeoclimatology, Palaeoecology 170, 237-260.

955 Mei, S.L., Zhang, K.X., Wardlaw, B.R., 1998. A refined succession of Changhsingian and
956 Griesbachian neogondolellid conodonts from the Meishan section, candidate of the
957 global stratotype section and point of the Permian-Triassic boundary.
958 Palaeogeography, Palaeoclimatology, Palaeoecology 143, 213-226.

959 Meyer, K.M., Ridgwell, A., and Kump, L.R., 2008. Biogeochemical controls on photic zone
960 euxinia during the end-Permian mass extinction. Geology 36(9), 747-750.

961 Meyer, K.M., Kump, L.R., 2008. Oceanic euxinia in Earth history: Causes and consequences.
962 Annual Review of Earth and Planetary Sciences 36, 251-288.

963 Meyer, K.M., Yu, M., Jost, A.B., Kelley, B.M., Payne, J.L., 2011. $\delta^{13}C$ evidence that high primary
964 productivity delayed recovery from end-Permian mass extinction. Earth and Planetary
965 Science Letters 302, 378-384.

966 Musashi, M., Isozaki, Y., Koike, T., Kreulen, R., 2001. Stable carbon isotope signature in mid-
967 Panthalassa shallow-water carbonates across the Permo-Triassic boundary: evidence
968 for ^{13}C-depleted superocean. Earth and Planetary Science Letters 191, 9-20.

969 Newton, R.J., Pevitt, E.L., Wignall, P.B., Bottrell, S.H., 2004. Large shifts in the isotopic
970 composition of seawater sulphate across the Permo-Triassic boundary in northern
971 Italy. Earth and Planetary Science Letters 218, 331-345.

Nielsen, J.K., Shen, Y., 2004. Evidence for sulfidic deep water during the Late Permian in the East Greenland Basin. Geology 32, 1037-1040.

Ogg, J. G., Ogg, G., Gradstein, F.M. 2008. The Concise Geologic Time Scale, Cambridge University Press

O'Leary, M.H., 1981. Carbon isotope fractionation in plants. Phytochemistry 20, 553-567.

O'Leary, M. H., 1988. Carbon isotopes in photosynthesis. Bioscience 38, 328-336.

Orchard, M.J., Krystyn, L., 1998. Conodonts of the lowermost Triassic of Spiti, and new zonation based on Neogondolella successions. Revista Italiana di Paleontologia Stratigraphia 104 (3), 341-368.

Orchard, M.J., Nassichuk, W.W., Rui, L., 1994. Conodonts from the Lower Griesbachian Otoceras latilobatum bed of Selong, Tibet and the position of the P-T boundary. Canadian Society of Petroleum Geologists. Proceedings of Pangea Conference Memoir, vol. 17, pp. 823-843.

Payne, J.L., Kump, L.R., 2007. Evidence for recurrent Early Triassic massive volcanism from quantitative interpretation of carbon isotope fluctuations. Earth and Planetary Science Letters 256, 264-277.

Payne, J.L., Lehrmann, D.J., Wei, J., Orchard, M.J., Schrag, D.P., Knoll, A.H., 2004. Large perturbations of the carbon cycle during recovery from the end-Permian extinction. Science 305, 506-509.

Peucker-Ehrenbrink, B., Ravizza, G., 2000. The marine osmium isotope record. Terra Nova 12, 205-219.

Radke, M., Welte, D.H., Willsch, H., 1982. Geochemical study on a well in the Western Canada Basin: relation of the aromatic distribution pattern to maturity of organic matter.

995 Geochimica et Cosmochimica Acta 46, 1-10.

996 Raup, D.M., Sepokoski, J.J., 1982. Mass extinction in the marine fossil record. Science 215,
997 1501-1503.

998 Reichow, M.K., Pringle, M.S., Al'Mukhamedov, A.I., Allen, M.B., Andreichev, V.L., Buslov, M.M.,
999 Davies, C.E., Fedoseev, G.S., Fitton, J.G., Inger, S., Medvedev, A.Y., Mitchell, C., Puchkov,
1000 V.N., Safanova, I.Y., Scott, R.A., Saunders, A.D., 2009. The timing and extent of the
1001 eruption of the Siberian Traps large igneous province: Implications for the end-
1002 Permian environmental crisis. Earth and Planetary Science Letters 277, 9-20.

1003 Reid, C.M., James, N.P., Beauchamp, B., Kyser, T.K., 2007. Faunal turnover and changing
1004 oceanography: late Palaeozoic warm-to-cool water carbonates, Sverdrup Basin,
1005 Canadian Arctic Archipelago. Palaeogeography, Palaeoclimatology, Palaeoecology 249,
1006 128-159.

1007 Retallack, G.J., 1999. Postapocalyptic greenhouse paleoclimate revealed by earliest Triassic
1008 paleosols in the Sydney Basin, Australia. Geol. Soc. Am. Bull. 111, 52-70.

1009 Retallack, G.J., Jahren, A.H., 2008. Methane release from igneous intrusion of coal during
1010 Late Permian extinction events. Journal of Geology 116, 1-20.

1011 Retallack, G.J., Smith, R.M.H., Ward, P.D., 2003. Vertebrate extinction across the Permian–
1012 Triassic boundary in Karoo Basin, South Africa. Geological Society of America Bulletin
1013 115, 1133-1152.

1014 Riccardi, A.L., Arthur, M.A., Kump, L.R., 2006. Sulfur isotopic evidence for chemocline
1015 upward excursions during the end-Permian mass extinction. Geochimica et
1016 Cosmochimica Acta 70, 5740-5752.

1017 Richards, B.C., 1989. Upper Kaskaskia Sequence: Uppermost Devonian and Lower
1018 Carboniferous. In: Ricketts, B. (ed.) Basin Analysis - The Western Canada Sedimentary
1019 Basin, Canadian Society of Petroleum Geologists Special Publication, pp. 165-201.

1020 Rooney, A.D., Selby, D., Houzay, J-P., Renne, P.R., 2010. Re-Os geochronology of
1021 Mesoproterozoic sediments from the Taoudeni basin, Mauritania: Implications for
1022 basin-wide correlations, supercontinent reconstruction and Re-Os systematics of
1023 organic-rich sediments. Earth and Planetary Science Letters 289, 486-496.

1024 Sano, H., Kuwahara, K., Yao, A., Agematsu, S., 2010. Panthalassic seamount-associated
1025 Permian-Triassic boundary siliceous rocks, Mino terrane, central Japan. Paleontological
1026 Research 14, 293-314.

1027 Schoepfer, S.D., Henderson, C.M., Garrison, G.H., Ward, P.D. 2012 Cessation of a productive
1028 coastal upwelling system in the Panthalassic Ocean at the Permian–Triassic Boundary,
1029 Palaeogeography, Palaeoclimatology, Palaeoecology 313–314, 181-188

1030 Seitzinger, S., Harrison, J.A., Böhlke, J.K., Bouwman, A.F., Lowrance, R., Peterson, B., Tobias,
1031 C., Van Drecht, G., 2006. Denitrification across landscapes and waterscapes: a synthesis.
1032 Ecological Applications 16, 2064–2090.

1033 Selby, D.A., Creaser, R.A., 2003. Re-Os geochronology of organic rich sediments: an
1034 evaluation of organic matter analysis methods. Chemical Geology 200, 225-240.

1035 Selby, D. 2007. Direct rhenium-osmium age of the oxfordian-kimmeridgian boundary,
1036 Staffin Bay, Isle of Skye, UK and the Late Jurassic geologic timescale. Norwegian Journal
1037 of Geology, 87, 291-299.

1038 Sephton, M.A., Looy, C.V., Brinkhuis, H., Wignall, P.B., de Leeuw, J.W., Visscher, H. 2005
1039 Catastrophic soil erosion during the end-Permian biotic crisis. Geology 33, 941-944

1040 Shen, S., Cao, C., Henderson, C.M., Wang, X., Shi, G.R., Wang, Y. and Wang, W., 2006. End-
1041 Permian mass extinction pattern in the northern peri-Gondwanan region. Palaeoworld
1042 15, 3-30.

1043 Shen, S.Z., Crowley, J.L., Wang, Y., Bowring, S.A., Erwin, D.H., Sadler, P.M., Cao, C.Q., Rothman,
1044 D.H., Henderson, C.M., Ramezani, J., Zhang, H., Shen, Y., Wang, X.D., Wang, W., Mu, L., Li,
1045 W.Z., Tang, Y.G., Liu, X.L., Liu, L.J., Zeng, Y., Jiang, Y.F., Jin, Y.-G. 2011. Calibrating the end-
1046 Permian mass extinction. Science 334, 1367-1372.

1047 Shen, S.Z., Henderson, C.M., Bowring, S.A., Cao, C.Q., Wang, Y., Wang, W., Zhang, H., Zhang,
1048 Y.C., Mu, L., 2010. High-resolution Lopingian (Late Permian) timescale of South China.
1049 Geological Journal 45, 122-134.

1050 Shen, Y., Farquhar, J., Zhang, H., Masterson, A., Zhang, T., Wing, B.A., 2011. Multiple S-
1051 isotopic evidence for episodic shoaling of anoxic water during Late Permian mass
1052 extinction. Nature Communications 2:210, 1-5.

1053 Smoliar, M. I., Walker, J.R., Morgan, J.W. 1996. Re-Os isotope constraints on the age of Group
1054 IIA, IIIA, IVA, and IVB iron meteorites. Science 271, 1099-1102.

1055 Song, H.Y., Tong, J.N., Algeo, T.J., Qiu, H.O., Song, H.J., Tian, L., Chen, Z.Q., in review. Large
1056 shallow-to-deep $\delta^{13}C$ gradients in Early Triassic seas of the South China craton:
1057 Evidence for elevated primary productivity and its role in sustaining oceanic anoxia
1058 and delaying marine ecosystem recovery following the end-Permian mass extinction.
1059 Global and Planetary Change, submitted October 2011.

1060 Song, H.Y., Tong, J.N., Algeo, T.J., Song, H.J., in review. Coupling of the marine carbon and
1061 sulfur cycles during the Early Triassic. Nature Geoscience, submitted November 2011.

1062 Strauss, H., 1999. Geological evolution from isotope proxy signals—sulfur. Chemical Geology
1063 161, 89-101.

1064 Sweet, W.C., 1970. Uppermost Permian and Lower Triassic conodonts of the Salt Range and
1065 Trans-Indus Ranges — West Pakistan. In: Kummel, B., Teichert, C. (eds.), Stratigraphic
1066 Boundary Problems: Permian and Triassic of West Pakistan. University of Kansas,
1067 Special Publications, vol. 4, pp. 207-275.

1068 Taylor, E.T., Taylor, T.N., Cúeno, R., 2000. Permian and Triassic high latitude paleoclimates:
1069 evidence from fossil biotas. In: Huber, B., Macleod, K. (eds.) Warm Climates in Earth
1070 History: Cambridge, Cambridge University Press, pp. 321-350.

1071 Tissot, B.P., Welte, D.H., 1984. Petroleum Formation and Occurrence, 2nd ed., Springer,
1072 Berlin, 699 pp.

1073 Tribovillard, N., Algeo, T.J., Lyons, T., Riboulleau, A., 2006. Trace metals as paleoredox and
1074 paleoproductivity proxies: An update. Chemical Geology 232, 12-32.

1075 Twitchett, R.J., Wignall, P.B., 1996. Trace fossils and the aftermath of the Permo-Triassic
1076 mass extinction: evidence from northern Italy. Palaeogeography, Palaeoclimatology,
1077 Palaeoecology 124, 137-151.

1078 Utting, J., Zonneveld, J.P., MacNaughton, R.B., Fallas, K.M., 2005. Palynostratigraphy,
1079 lithostratigraphy and thermal maturity of the Lower Triassic Toad and Grayling, and
1080 Montney formations of western Canada, and comparisons with coeval rocks of the
1081 Sverdrup Basin, Nunavut. Bulletin of Canadian Petroleum Geology 63, 5-24.

1082 Ward, P.D., Montgomery, D.R., Smith, R., 2000. Altered river morphology in South Africa
1083 related to the Permian-Triassic extinction. Science 289, 1740-1743.

1084 Ward, P.D., Botha, J., Buick, R., De Kock, M.O., Erwin, D.H., Garrison, G., Kirschvink, J., Smith,

1085 R., 2005. Abrupt and Gradual Extinction Among Late Permian Land Vertebrates in the
1086 Karoo Basin, South Africa. www.sciencexpress.org / 20 January 2005 / Page 1/
1087 10.1126/science.1107068.

1088 Werne, J.P., Lyons, T.W., Hollander, D.J., Formolo, M.J., Sinninghe Damsté, J.S., 2003. Reduced
1089 sulfur in euxinic sediments of the Cariaco Basin: sulfur isotope constraints on organic
1090 sulfur formation. Chemical Geology 195, 159-179.

1091 White, R.V., 2002. Earth's biggest 'whodunnit': unravelling the clues in the case of the end-
1092 Permian mass extinction: Philosophical Transactions of the Royal Society of London,
1093 Series B, 360, 2963-2985.

1094 Wignall, P.B., 2007. The End-Permian mass extinction—how bad did it get? Geobiology 5,
1095 303-309.

1096 Wignall, P.B., Hallam, A., 1992. Anoxia as a cause of the Permian/Triassic mass extinction:
1097 facies evidence from northern Italy and the western United States. Palaeogeography,
1098 Palaeoclimatology, Palaeoecology 93, 21-46.

1099 Wignall, P.B., Hallam, A., 1993. Griesbachian (Earliest Triassic) palaeoenvironmental
1100 changes in the Salt Range, Pakistan and southeast China and their bearing on the
1101 Permo-Triassic mass extinction. Palaeogeography, Palaeoclimatology, Palaeoecology
1102 102, 215-237.

1103 Wignall, P.B., Newton, R., 1998. Pyrite framboid diameter as a measure of oxygen deficiency
1104 in ancient mudrocks. American Journal of Science 298, 537-552.

1105 Wignall, P.B., Newton, R. 2003. Contrasting deep-water records from the Upper Permian
1106 and Lower Triassic of South Tibet and British Columbia: evidence for a diachronous
1107 mass extinction. Palaios 18, 153-167.

1108 Wignall, P.B., Twitchett, R.J., 1996. Oceanic anoxia and the end Permian mass extinction.
1109 Science 272, 1155-1158.

1110 Wignall, P.B., Twitchett, R.J., 2002. Extent, duration, and nature of the Permian-Triassic
1111 superanoxic event. In: Koeberl, C., MacLeod, K.G. (eds.), Catastrophic Events and Mass
1112 Extinctions: Impacts and Beyond. Geological Society of America Special Paper 356, pp.
1113 395-413.

1114 Wilkin, R.T., Arthur, M.A., 2001. Variations in pyrite texture, sulfur isotope composition, and
1115 iron systematics in the Black Sea: Evidence for late Pleistocene to Holocene excursions
1116 of the O2-H2S redox transition. Geochimica et Cosmochimica Acta 65, 1399-1416.

1117 Wilkin, R.T., Barnes, H.L., Brantley, S.L., 1996. The size distribution of framboidal pyrite in
1118 modern sediments: an indicator of redox conditions. Geochimica et Cosmochimica Acta
1119 60, 3897-3912.

1120 Winguth, A.M.E., Heinze, C., Kutzbach, J. E., Maier-Reimer, E., Mikolajewicz, U., Rowley, D.,
1121 Rees, A., and Ziegler, A. M., 2002. Simulated warm polar currents during the middle
1122 Permian, Paleoceanography 17(4), 1057, doi:10.1029/2001PA000646.

1123 Winguth, A.M.E., Maier-Reimer, E., 2005. Causes of marine productivity and oxygen changes
1124 associated with the Permian-Triassic boundary: A reevalution with ocean general
1125 circulation models. Marine Geology 217, 283-304.

1126 Yin, H.F., Sweet, W.C., Glenister, B.F., Kotlyar, G., Kozur, H., Newell, N.D., Sheng, J.Z., Yang, Z.Y.,
1127 Zakharov, Y.D., 1996. Recommendation of the Meishan section as Global Stratotype
1128 Section and Point for basal boundary of Triassic system. Newsletter on Stratigraphy 34,
1129 81-108.

1130 Yin, H.F., Zhang, K.X., Tong, J.N., Yang, Z.Y., Wu, S.B., 2001. The Global Stratotype Section and
1131 Point (GSSP) of the Permian–Triassic boundary. Episodes 24, 102-114.

1132 Zhang, K., Tong, J., Shi, G.R., Lai, X., Yu, J., He, W., Peng, Y., Jin, Y., 2007. Early Triassic
1133 conodont-palynological biostratigraphy of the Meishan D section in Changxing,
1134 Zhejiang Province, South China. Palaeogeography, Palaeoclimatology, Palaeoecology
1135 252, 4-23.

1136 Ziegler A.M., Gibbs M.T., Hulver M.L., 1998. A mini-atlas of oceanic water masses in the
1137 Permian period. Proceedings of the Royal Society of Victoria 110 (1/2), 323– 343.

1138

1139

1140

1141 **Figure and Table captions**

1142

1143 **Figure 1.** (A) Late Permian paleogeography, showing the major ocean basins and location
1144 of the Opal Creek section. Map generated by PaleoDB.org, Alroy 2010. (B) Map of Canada
1145 showing the location of the Kananaskis Valley in southwestern Alberta. (C) Map showing
1146 the location of the Opal Creek section in the Kananaskis Valley.

1147 **Figure 2.** (A) Photograph of Opal Creek outcrop from approach. Note cliff-forming, silicified
1148 Ranger Canyon and less resistant Sulphur Mountain silts exposed in hillside. The cliff
1149 face corresponds to the unconformity. (B) Close up of Permian-Triassic boundary.
1150 Pyrite bed weathers to reddish in outcrop. RC = Ranger Canyon Formation, SM =
1151 Sulphur Mountain Formation, SB = unconformable Sequence Boundary, Py. = Pyrite
1152 layer, Ext. = main extinction horizon.

Figure 3. Stratigraphic column with lithostratigraphy as well as isotopic and trace element records for the Opal Creek section. Heavy red line corresponds to the biostratigraphic PTB, the thin red line corresponds to the main marine extinction event. The number of samples analyzed for each proxy is as follows: $\delta^{13}C_{org}$, n = 191, $\delta^{15}N$, n = 58, $\delta^{34}S$, n = 56 acidified (n = 7 acidified+bleached), %S, n = 55, TOC, n = 185, All trace element proxies, n = 29.

Figure 4. Expanded stratigraphic column for 4.5-m-thick interval of the Opal Creek section bracketing the unconformity and PTB, with isotope measurements and calculated initial osmium isotope ratios (*I*Os, see Re-Os Analysis in Results section). Solid red line indicates the biostratigraphic PTB, the dashed red line indicates the main extinction event. *M. bitteri* zone overlaps with *M. rosenkrantzi* in uppermost 5-10 cm of Ranger Canyon Formation. The number of measurements shown for each proxy is as follows: $\delta^{13}C_{org}$, n = 149, $\delta^{15}N$, n = 41, $\delta^{34}S$, n = 36 acidified (n = 2 acidified+bleached), *I*Os, n = 14.

Figure 5. (A) TOC versus total S. The majority of samples falls along the oxic-suboxic trend of Berner and Raiswell (1983). A subset of samples (n ~12) plots distinctly above the oxic-suboxic trend; they represent the basal 4 m of the SMF plus a few pyritic layers higher in the section. (B) Total S versus pyrite $\delta^{34}S$. Note that high-S samples are low in TOC and enriched in ^{34}S. Samples shown in this figure are a separate set processed at the U. of Cincinnati.

Figure 6. Reflected light petrographic photomicrographs of SMF: (A) Massive pyrite in calcareous silicate matrix. (B) Massive marcasite in silicate matrix. (C) Medium-sized (8-12 μm) pyrite framboids with partial diagenetic overgrowths. (D) Coarse euhedral and

irregular diagenetic pyrite masses. (E) Large (35 μm) pyrite framboid with diagenetic overgrowths. (F) Fine (3-10 μm) diagenetic pyrite crystals in a large organic particle. (G) Fine diagenetic pyrite within a diagenetic calcite crystal. (H) Variably sized (4-20 μm) pyrite framboids along an organic-rich lamina. (J) Coarse diagenetic pyrite associated with diagenetic carbonate crystals. (K) Coarse diagenetic pyrite within a carbonate nodule. (L) Variably sized (10-40 μm) pyrite framboids along an organic-rich lamina. (M) Organic particle with diagenetic pyrite overgrowths (lower left) and blocky diagenetic pyrite (upper right). (N) Fine (4-12 μm) pyrite framboids along an organic-rich lamina. (O) Coarse (20-40 μm) pyrite framboids with diagenetic overgrowths on larger framboid. (P) Fine (3-8 μm) diagenetic pyrite crystals in an organic particle.

Figure 7. Integrated model of environmental conditions on the subtropical eastern Panthalassic margin (A) During the Early and Middle Permian (B) During the main latest Permian extinction interval (C) During the earliest Triassic

Table 1. Concentrations and enrichment factors of some major and trace elements

†AUCC = Average Upper Continental Crust (McLennan 2001)

Table 2. Re and Os concentrations and isotopes. *I*Os uncertainties were less than or equal to .004**.**

†Initial osmium compositions (*I*Os) calculated for an age of 252.2 Ma.

1184 Figure 1

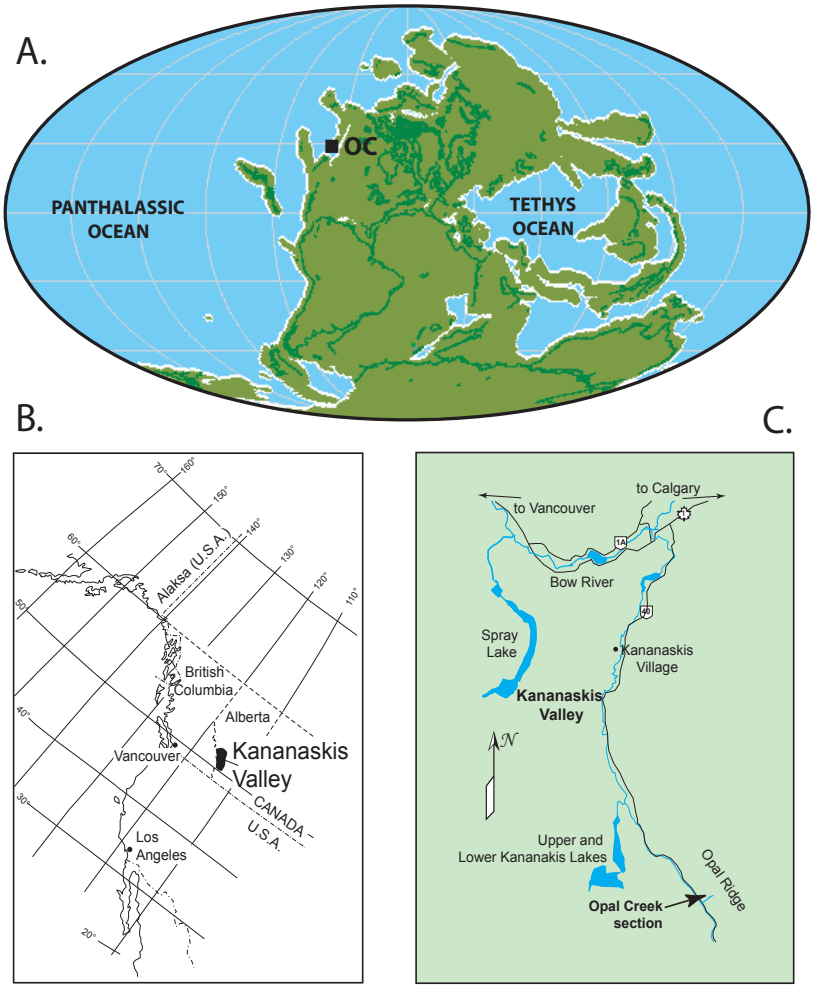

1185

1186 Figure 2

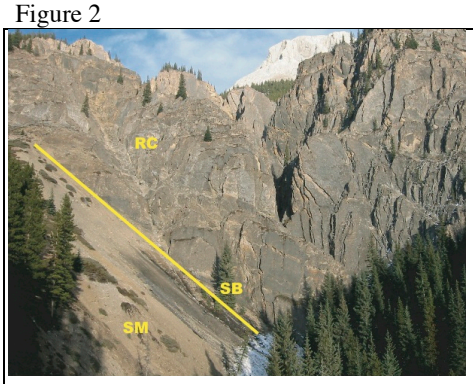

A.

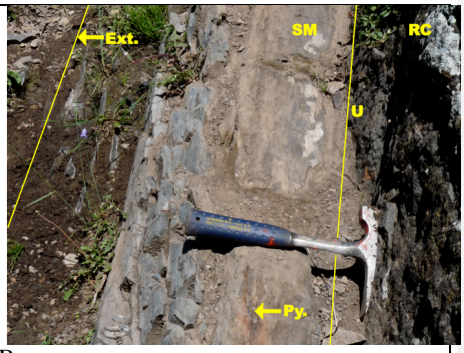

B.

1187

1188 Figure 3

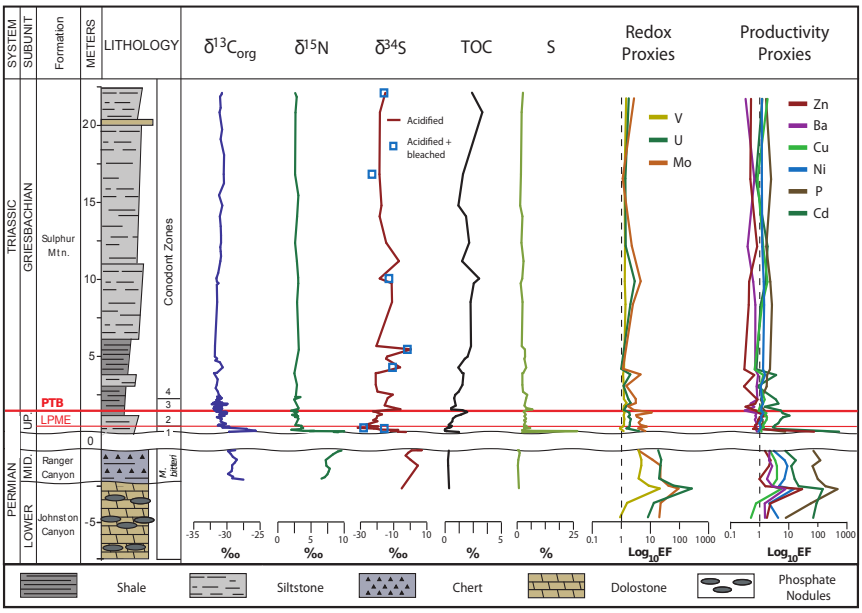

1189

Figure 4.

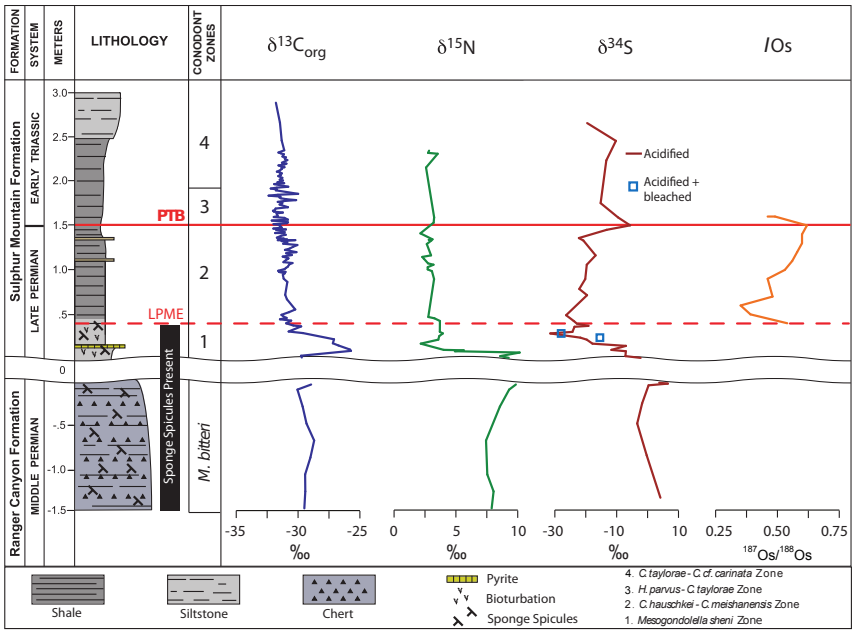
FORMATION
SYSTEM
METERS
LITHOLOGY
CONODONT ZONES
δ13Corg
δ15N
δ34S
IOs
Sulphur Mountain Formation
EARLY TRIASSIC
LATE PERMIAN
Ranger Canyon Formation
MIDDLE PERMIAN
PTB
LPME
Sponge Spicules Present
M. bitteri
Acidified
Acidified + bleached
‰
187Os/188Os
Shale
Siltstone
Chert
Pyrite
Bioturbation
Sponge Spicules
4. C.taylorae - C.cf. carinata Zone
3. H.parvus - C.taylorae Zone
2. C.hauschkei - C.meishanensis Zone
1. Mesogondolella sheni Zone

1214 Figure 5.
1215

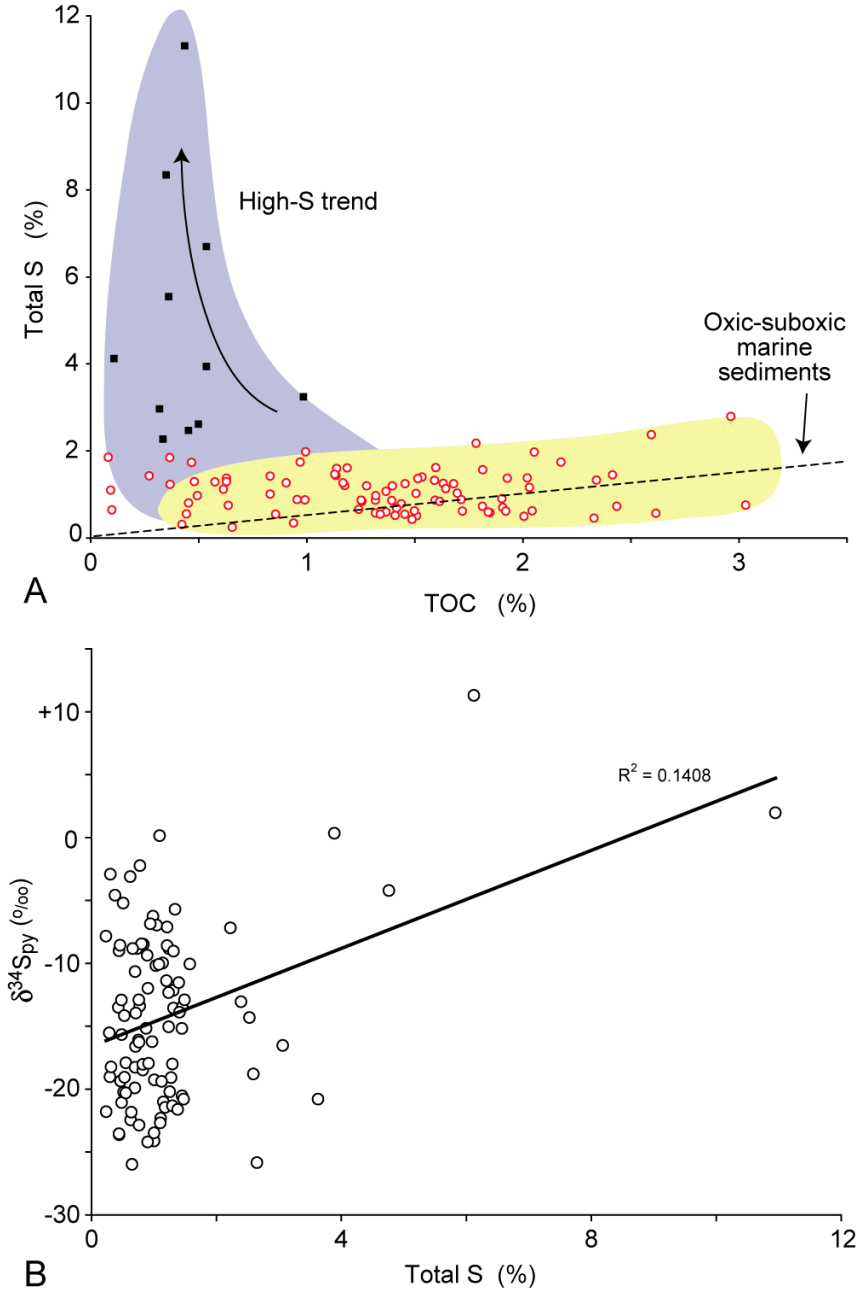

1216

Figure 6.

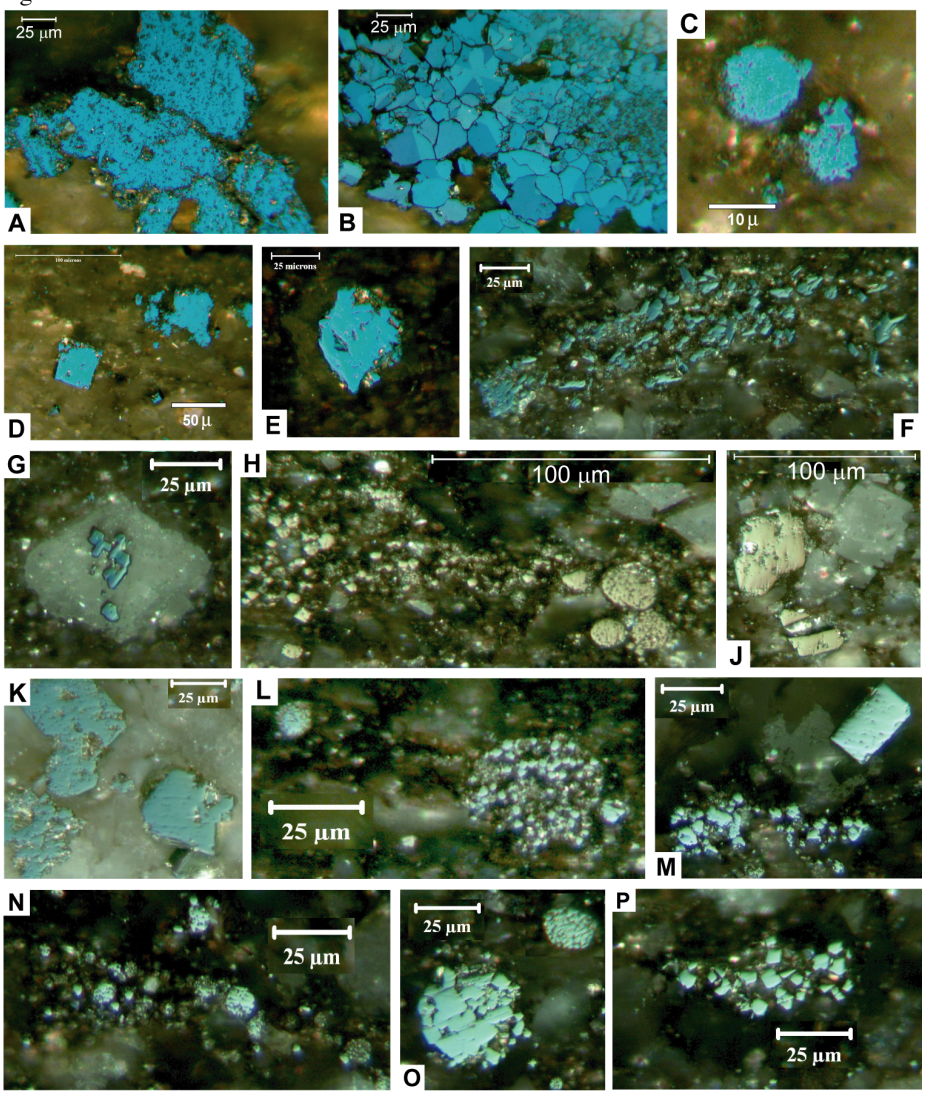
25 µm
A
25 µm
B
C
10 µ
50 µ
D
25 microns
E
25 µm
F
G
25 µm
H
100 µm
100 µm
J
K
25 µm
L
25 µm
25 µm
M
N
25 µm
25 µm
O
P
25 µm

1227 Figure 7.

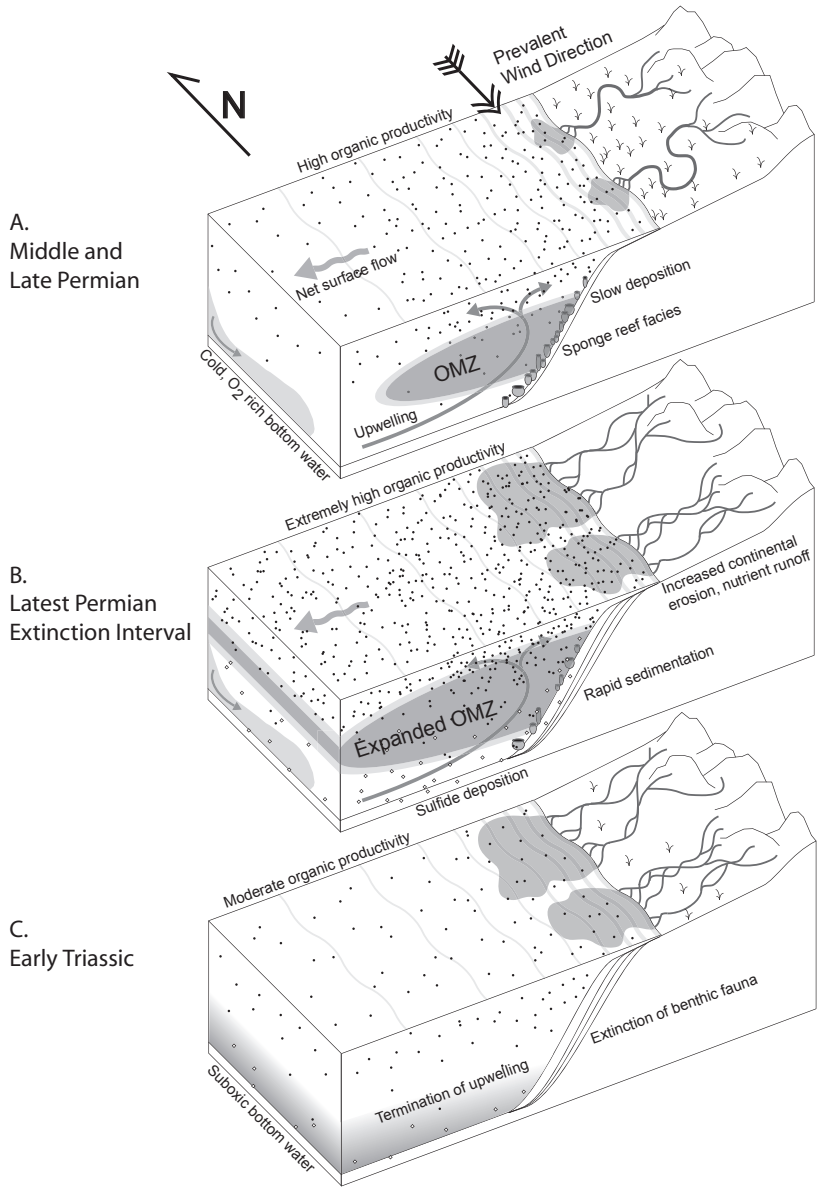

1228